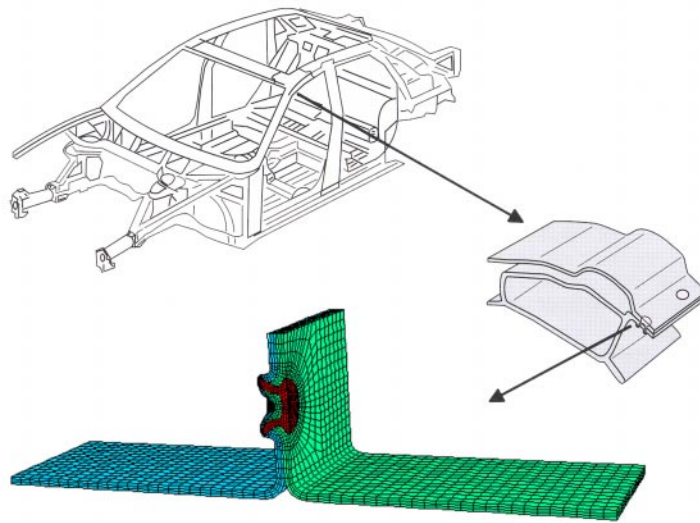




LUND
UNIVERSITY



FINITE ELEMENT SIMULATION OF CRASH TESTING OF SELF-PIERCING RIVET JOINTS, PEEL SPECIMEN

CHRISTIAN WESTERBERG

Structural
Mechanics

Master's Dissertation

Structural Mechanics

ISRN LUTVDG/TVSM--02/5116--SE (1-57)

ISSN 0281-6679

FINITE ELEMENT SIMULATION OF
CRASH TESTING OF SELF-PIERCING
RIVET JOINTS, PEEL SPECIMEN

Master's Dissertation by
CHRISTIAN WESTERBERG

Supervisors:

ERIK SERRANO, Div. of Structural Mechanics
ARNE MELANDER, Institute for Metals Research

Copyright © 2002 by Structural Mechanics, LTH, and Institute for Metals Research, Sweden.
Printed by KFS I Lund AB, Lund, Sweden, September, 2002.

For information, address:
Division of Structural Mechanics, LTH, Lund University, Box 118, SE-221 00 Lund, Sweden.
Homepage: <http://www.byggmek.lth.se>

Preface

The work presented in this master's dissertation was performed during the spring and summer of 2002. It is a required part in obtaining the degree of Master of Science in civil engineering. The work is valued to 20 credits, corresponding to 20 weeks of full-time work.

The present project was financed by the Swedish Institute for Metal Research (SIMR). This support is gratefully acknowledged. Great gratitude to Prof. Arne Melander and Dr. Anders Thuvander for advice, help and guidance during the course of the work whenever needed.

Thanks also to the Division of Structural Mechanics, Lund Institute of Technology, for accepting the graduate work, and especially Dr. Erik Serrano and Prof. Göran Sandberg, who approved it.

Finally I would like to thank all the staff at SIMR who helped and guided me through the work, and for making my time at SIMR pleasant.

Christian Westerberg

Abstract

Within the automotive industry today, companies save significant amounts of money through computer simulations. Mathematics through numerical methods becomes important when as in this case the investigation is done with the Finite Element Method (FEM). A self-pierced rivet (SPR) joint specimen in a T-peel case is studied. The specimen consists of 1.15 mm thick steel sheets with a rivet of 5 mm in waist-diameter.

The simulations are performed with the finite element software ABAQUS/Explicit, and involve dynamic inertia effects. The Johnson-Cook plasticity model is used to describe the materials, a deep drawing quality (DDQ) and a dual phase (DP600) steel.

Different parameter variations are made. These are for example velocity, friction and material. Displacement velocities of 1, 10, 25 and 100 m/s are evaluated. The results are compiled and assembled to load- and energy-curves. The curves are then compared with the visual deformation process of the specimen. Comparisons with spot- and laser-welded joints are also done.

Some results are:

- The deformation process was more or less similar at 1, 10 and 25 m/s.
- Higher velocity results in higher load levels, higher energy and larger failure displacement.
- The DDQ steel shows lower load levels and larger failure displacement than the DP600 steel at all velocities.
- The load-displacement curves are quite similar for the spot-welded and SPR cases, except for the oscillating amplitudes where SPR is larger.

Table of Contents

1. INTRODUCTION	7
2. SELF-PIERCING RIVETING	9
2.1 THE RIVET PROCESS	10
2.2 JOINT REQUIREMENTS	11
3. BACKGROUND TO NUMERICAL SOLUTION PROCEDURES AND FE SIMULATIONS ...	13
3.1 THE FINITE ELEMENT METHOD	13
3.2 EXPLICIT METHOD	13
3.2.1 <i>Central difference method</i>	14
3.3 THE FE PROGRAM - ABAQUS.....	15
3.4 JOHNSON-COOK PLASTICITY MODEL	15
4. FE MODEL - INPUT DATA	17
4.1 GEOMETRY AND MESH	17
4.1.1 <i>Geometry model</i>	17
4.1.2 <i>Mesh</i>	18
4.1.3 <i>Choice of element</i>	20
4.1.4 <i>Contact interaction</i>	21
4.2 MATERIAL DATA.....	21
4.3 BOUNDARY CONDITIONS AND LOADING	23
4.3.1 <i>Boundary conditions</i>	23
4.3.2 <i>Loading</i>	24
5. RESULTS FROM FE SIMULATION	25
5.1 REFERENCE CASE.....	26
5.1.1 <i>Load</i>	26
5.1.2 <i>Energy</i>	28
5.2 INFLUENCE OF VELOCITY	30
5.3 INFLUENCE OF FRICTION	36
5.4 INFLUENCE OF MATERIAL.....	38
5.4.1 <i>Comparison of the sheet steels DDQ and DP600</i>	38
5.4.2 <i>Influence of strain rate sensitivity</i>	41
5.4.3 <i>Influence of rivet strength</i>	42
5.5 INFLUENCE OF CRACKING	42
5.6 INFLUENCE OF SPECIMEN LENGTH.....	43
5.7 INFLUENCE OF DOUBLE SYMMETRY	44
5.8 INFLUENCE OF LOAD APPLICATION.....	45
5.8.1 <i>Tabular</i>	45
5.8.2 <i>Smooth</i>	46
5.9 INFLUENCE OF SOLVER PRECISION.....	47
6. COMPARISON WITH OTHER JOINTS	49
6.1 COMPARISON WITH SPOT WELDED JOINTS	49
6.2 COMPARISON WITH LASER WELDED JOINTS.....	53
7. CONCLUSIONS	55
8. FURTHER WORK	55
9. REFERENCES	57

1. Introduction

Within the automotive industry today, companies save significant amounts of money through computer simulations. Computer simulations are used for example to test crashworthiness, with a goal to increase the safety in cars. This is done because it is cheaper to crash a car “inside” the computer than in reality. This has led to great concentration on numerical calculations.

Essentially all phenomena, which describe a process that involves some kind of variation, can be described by means of differential equations. Mathematics becomes then the natural means to understand and describe such a phenomenon, and to interpret and solve them. Effective and reliable numerical models are necessary to be able to optimize weight, production costs and structural strength.

The joints that join different parts in a car body are often the weakest points as regards to structural strength. They can break due to fatigue or by extreme forces, like a crash. A car body contains many joints, so a full car model must be simple enough to give reasonable demands on the computers’ memory and speed.

Self-piercing rivets (SPR) are becoming more and more common as joining method in cars. For frame structures of aluminium SPR is already the dominant joining technique, see Audi A2 and A8. It is important that the rivet joints don’t separate while submitted to crash load so that an unstable collapse of the car body structure can be avoided.

In this report an advanced numerical calculation is done on a single rivet to give information that makes it possible to make simplified but yet realistic models on full car structures. It is investigated how SPR deform with crash load. The influence of material parameters on load-response and energy-consumption is studied. This is done on a T-peel specimen. The studies have, among other things, lead to a good understanding of what parameters that are crucial for the structural strength.

The finite element method (FEM) is today the most widely used technique for computer-based analysis of problems within mechanics of materials. The method started to develop in the 50’s and has developed ever since. Today it is possible to analyse three-dimensional geometry with consideration of both large deformations and non-linear material behaviour (e.g. plasticity). In this work, finite element calculations are performed using the software ABAQUS/Explicit.

To carry out a complete FEM-calculation the following steps must be taken.

- Create appropriate geometry.
- Meshing and specify elements.
- Apply loads and boundary conditions.
- Perform solution.
- Study and estimation/evaluation of the results.
- Documentation.

2. Self-piercing riveting

Self-piercing riveting (SPR) is a method of joining two pieces of material using a rivet (see figure 2.1 and 2.2). Unlike conventional riveting, self-piercing riveting does not require a pre-drilled hole, because the rivet makes its own hole as it is being inserted. This brings great benefits in terms of production cost reduction and ease of use compared to conventional riveting.

The increasing use of coated, lightweight and high-strength materials, such as galvanised or pre-painted steel and aluminium has led industries to re-examine traditional methods of assembling components. As welding of these materials is difficult or impossible, and assembly using conventional rivets is slow and costly, the benefits of a process that combines high joint integrity with rapid assembly times become obvious [9].



Figure 2.1. T-peel specimen of SPR-joints.

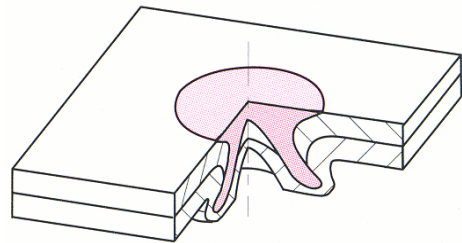


Figure 2.2. A self-pierced rivet in cross section.

Self-piercing riveting has a number of advantages over more conventional joining techniques, such as spot welding and blind riveting:

- Joins a range of materials such as steel, aluminium and plastics.
- No hole required.
- No heat, fumes, dust or swarf given off.
- Doesn't burn zinc or painted coatings.
- Fast cycle time.
- Low noise operation.
- Repeatable quality, visually checkable joint with one shot operation.
- Automatic rivet feed for continuous production.
- Compatible with adhesives and lubricants.

Self-piercing rivets are, for example, used for 70% of the single point fastenings on the Audi A8, due to superior fatigue and crash worthiness of the joints compared with spot welding.

2.1 The rivet process

The self-piercing rivet is squeezed at high force into the material to be joined, piercing the top sheets of material and spreading outwards into the bottom sheet of material, under the influence of an upsetting die, to form a strong joint. Also see figure 2.2 and 2.3 below.

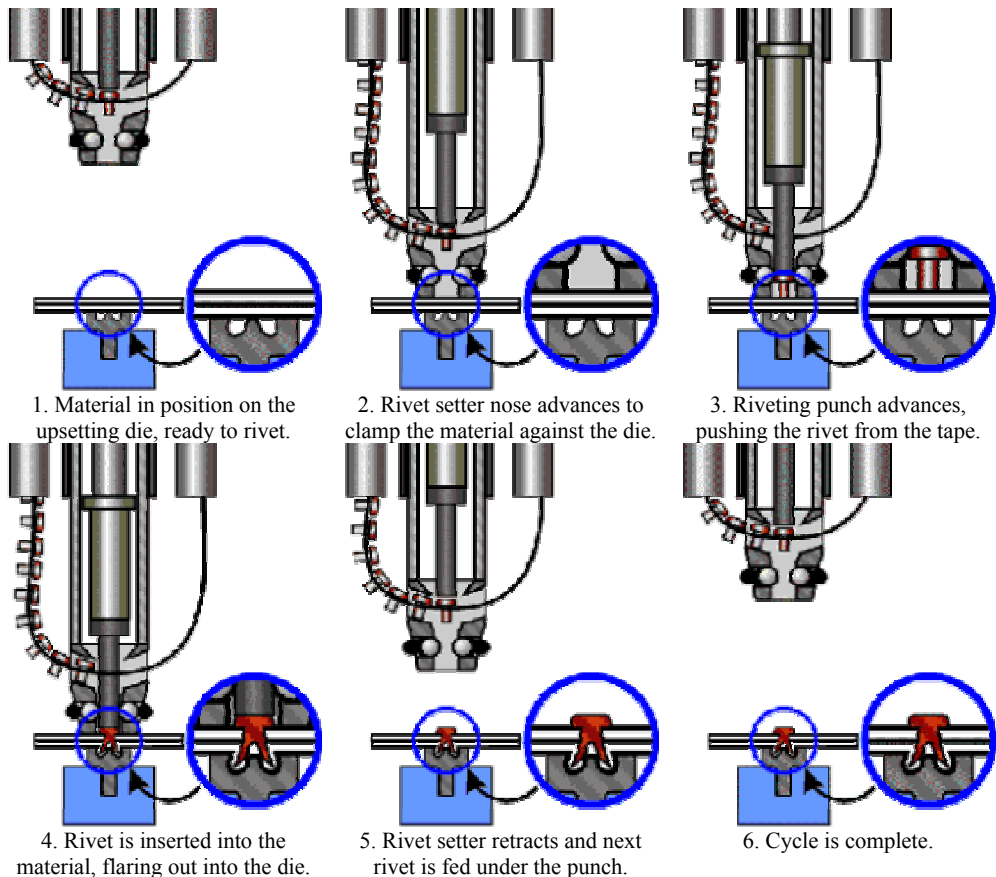


Figure 2.2. Description of a rivet setting operation with the Henrob process [9].

The rivet setting tool is powered hydraulically from a separate power pack, which also controls the tool sequencing. Rivets are fed automatically into the setting tool on a plastic belt, thus allowing automated, high volume production.

The rivet in this report is a countersunk rivet. In figure 2.3 there is another description of the rivet setting process.

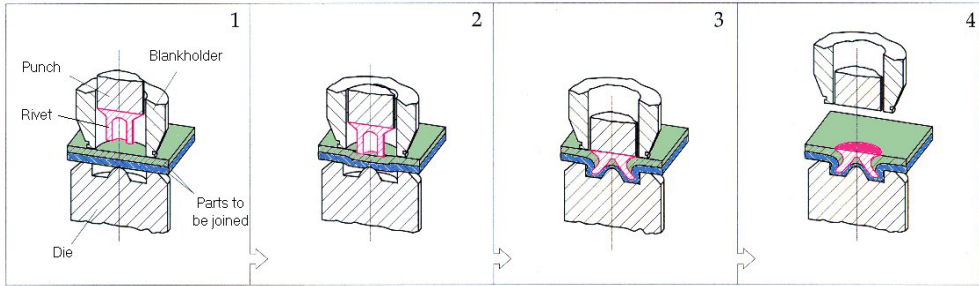


Figure 2.3. A simple general description of a countersunk rivet process.

2.2 Joint requirements

In order to have a satisfactory rivet joint, the requirements specified below must be complied with. The requirements apply to each individual self-piercing rivet in the joint.

For the punch side:

- the surface of the rivet head shall be parallel with the sheet metal surface
- in the case of countersunk rivets, the rivet head may be max. 0.2 mm above the sheet metal surface
- in the case of countersunk rivets, the rivet head may be max. 0.1 mm below the sheet metal surface.

For the die side:

- a fully shaped button shall show an outer diameter corresponding to the inside dimension of the die tool
- no breakthrough of the rivet permitted
- no cracks in the sheet permitted
- the remaining sheet thickness shall be min. 0.2 mm.

All this requirements are fulfilled in this investigation.

Above requirements according to VCS [10].

3. Background to numerical solution procedures and FE simulations

3.1 The finite element method

Most physical phenomena encountered in engineering mechanics are modelled by differential equations, and usually the problem is too complicated to be solved by classical analytical methods. The finite element method (FEM) is a numerical approach by which general differential equations can be solved in an approximate manner.

The differential equation or equations, which describe the physical problem considered, are assumed to hold over a certain region. This region may be one-, two- or three-dimensional, and in this investigation it's a three-dimensional problem. It is a characteristic feature of the finite element method that instead of seeking approximations that hold directly over the entire region, the region is divided into smaller parts, so-called finite elements, and the approximation is then carried out over each element. The elements may be all of the same size or all different. The collection of all elements is called a finite element mesh. The elements are interconnected only at nodes or nodal points. The nodal points are the ends of the element, and each node has a number of degrees of freedom (DOF). The DOF's represent in this report the displacement in all directions (x, y, z), i.e. three degrees of freedom at each node.

When the type of approximation that is to be applied over each element has been selected, and the mechanical behaviour of the material is known, the corresponding mechanical behaviour of each element can be determined. This can be performed because the approximation made over each element is quite simple. Having determined the behaviour of all elements, these elements are then patched together, using some specific rules, to form the entire region, which eventually enables us to obtain an approximate solution for the behaviour of the entire body [1].

The finite element method can accordingly be applied to obtain approximate solutions for arbitrary differential equations.

3.2 Explicit method

Analytical solutions of the equation of motion, equation (3.1) below, are usually not possible if the excitation varies arbitrarily with time or if the system is non-linear, like this case. Such problems can be tackled by numerical time-stepping methods for integration of differential equations. Ordinary differential equations can be numerically integrated with either an implicit or an explicit method. Both can be used in static and dynamic analyses, but the present case is treated as being dynamic.

The differences between the methods make them suitable at varying situations. Explicit methods demand less storage capacity and computer-time as compared to implicit method, which is due to the following:

- Explicit methods use diagonal, lumped mass matrices, so that the system to be solved is uncoupled.

- In the explicit method, no equilibrium iterations like Newton-Raphson are needed.

The convergence problem that emerges using implicit methods can often be avoided with an explicit method. The explicit method is suitable for fast dynamic processes and non-linear analyses such as crash simulations, i.e. perfect for the simulation in this report.

3.2.1 Central difference method

The explicit time integration method used in ABAQUS/Explicit is the central difference method [4]. The equilibrium is expressed at an instant when the displacements are known. By using this information, new equilibrium data can be calculated for the next time step. The implication of the method is that known information between the previous time step and the current are used to calculate the equilibrium at current time step. For a short derivation, see below.

The equation of motion can be written:

$$m\ddot{u}_i + c\dot{u}_i + ku_i = p_i \quad (3.1)$$

m , c and k are mass, damping and stiffness matrices and p is the applied force vector. u , \dot{u} and \ddot{u} are displacement, velocity and acceleration vectors respectively. For the next step the equation reads:

$$m\ddot{u}_{i+1} + c\dot{u}_{i+1} + ku_{i+1} = p_{i+1} \quad (3.2)$$

This method is based on a finite difference approximation of the time derivatives of displacement (\dot{u} and \ddot{u}). Taking constant time steps, $\Delta t_i = \Delta t$, the central difference expressions for velocity and acceleration at time i are

$$\dot{u}_i = \frac{u_{i+1} - u_{i-1}}{2\Delta t} \quad (3.3)$$

$$\ddot{u}_i = \frac{u_{i+1} - 2u_i + u_{i-1}}{(\Delta t)^2} \quad (3.4)$$

Substituting these approximate expressions for velocity and acceleration into eq. (3.1) gives

$$m \frac{u_{i+1} - 2u_i + u_{i-1}}{(\Delta t)^2} + c \frac{u_{i+1} - u_{i-1}}{2\Delta t} + ku_i = p_i \quad (3.5)$$

In this equation u_i and u_{i-1} are assumed known (from the preceding time steps).

Transferring these known quantities to the right-hand side leads to

$$\left[\frac{m}{(\Delta t)^2} + \frac{c}{2\Delta t} \right] u_{i+1} = p_i - \left[\frac{m}{(\Delta t)^2} - \frac{c}{2\Delta t} \right] u_{i-1} - \left[k - \frac{2m}{(\Delta t)^2} \right] u_i \quad (3.6)$$

or

$$\hat{k} u_{i+1} = \hat{p}_i \Rightarrow u_{i+1} = \hat{p}_i \cdot \hat{k}^{-1} \quad (3.7)$$

The solution u_{i+1} at time $i+1$ is determined from the equilibrium condition, eq. (3.1), at time i without using the equilibrium condition, eq. (3.2), at time $i+1$. Such a method is called an *explicit method* and is especially easy to implement on the computer [2].

Other methods are for example Newmark and Wilson's method.

The size of a time step, or a time increment (Δt), is of importance in terms of stability demands. If Δt is larger than the time for a dilatational wave to cross any of the elements, errors will appear. It can even stop the simulation. The mesh density is therefore very important. Smaller element sizes leading to smaller time steps and thus larger number of increments and computational cost.

3.3 The FE program - ABAQUS

The simulations are performed using ABAQUS (version 6.2), a finite element software. The ABAQUS finite element system includes:

- ABAQUS/CAE, an interactive pre-processor that can be used to create finite element models, the input file for ABAQUS/Standard and ABAQUS/Explicit,
- ABAQUS/Standard, a general-purpose finite element solver-program,
- ABAQUS/Explicit, an explicit dynamic finite element solver-program, and
- ABAQUS/Viewer, a menu-driven interaction post-processor that provides xy-plots, animations, contour plots and tabular output data of results.

In the present study all these program modules, except Standard, have been used to investigate the self-piercing rivet joints.

3.4 Johnson-Cook plasticity model

In order to describe the plastic and rate dependent hardening of the material the Johnson Cook model is used.

The Johnson-Cook plasticity model [4]:

- Is a particular type of Mises plasticity model with analytical forms of the hardening law and rate dependence,
- Is suitable for high-strain-rate deformation of many materials, including most metals, and
- Is typically used in adiabatic transient dynamic simulations.

When a material is loaded beyond its elastic limit, plastic deformation, an irreversible process, ensues. A yield criterion is required to assess whether or not yielding or plastic deformation is imminent or has occurred. One of the most widely used yield criteria is the *von Mises* yield condition, which is applied in ABAQUS. Its yield function is dependent upon the strain history for a work hardening material.

The yield stress is expressed as

$$\sigma = \underbrace{(A + B \cdot \varepsilon_{pl}^n)}_{static} \cdot \underbrace{\left(1 + C \cdot \ln\left(\frac{\dot{\varepsilon}_{pl}}{\dot{\varepsilon}_0}\right)\right)}_{dynamic} \cdot \underbrace{(1 - \hat{\theta}^m)}_{temperature} \quad (3.8)$$

This model is uncoupled, i.e. it deals with ε , $\dot{\varepsilon}$ and $\hat{\theta}$ independent of each other. A, B, n, C and m are constants that are determined from experiments. The temperature parameter is further explained below.

$$\begin{aligned} \hat{\theta} &= 0 & \text{for} & \quad \theta < \theta_{transition} \\ \hat{\theta} &= \frac{\theta - \theta_{transition}}{\theta_{melt} - \theta_{transition}} & \text{for} & \quad \theta_{transition} \leq \theta \leq \theta_{melt} \\ \hat{\theta} &= 1 & \text{for} & \quad \theta > \theta_{melt} \end{aligned}$$

θ is the current temperature of the specimen. The temperature parameter $(1 - \hat{\theta}^m)$ is in this investigation equal to one, thus the model is simulated in normal temperature, and has thereby no effect in the material model. To simulate this, the transition temperature is set high which makes the temperature to always be lesser than the transition temperature. The yield stress can then be written:

$$\sigma = (A + B \cdot \varepsilon_{pl}^n) \cdot \left(1 + C \cdot \ln\left(\frac{\dot{\varepsilon}_{pl}}{\dot{\varepsilon}_0}\right)\right) \quad (3.9)$$

σ = Yield stress (Pa)

C = Strain rate-hardening coefficient

A = Initial yield stress at $\dot{\varepsilon}_0$ (Pa)

$\dot{\varepsilon}_{pl}$ = Time derivative of effective plastic strain

B = Strain hardening coefficient (Pa)

$\dot{\varepsilon}_0$ = Reference strain rate sensitivity constant

ε_{pl} = Effective plastic strain

n = Strain hardening exponent

The stresses and strains refer to von Mises effective values.

4. FE model - input data

To create a model of the peel specimen ABAQUS/CAE was used [3]. This chapter describes the different steps in the creating process. The model consists of one rivet with its surroundings.

4.1 Geometry and mesh

4.1.1 Geometry model

The geometry of the rivet region was made in another report [8] from an image. Measurements were done and imported to ABAQUS/CAE. The image represents a result from a FE simulation done in the software tool DEFORM-2D and can be seen in figure 4.1 [5]. The figure is only 2-dimensional but it is rotational symmetric which contributes to the 3-dimensional model.

The sheets were then made to fit the peel specimen model. To simplify the model, a symmetry plane along the specimen was used, which splits the rivet in the middle. This procedure will reduce the number of elements and also decrease the computer-time (CPU-time), when solving.

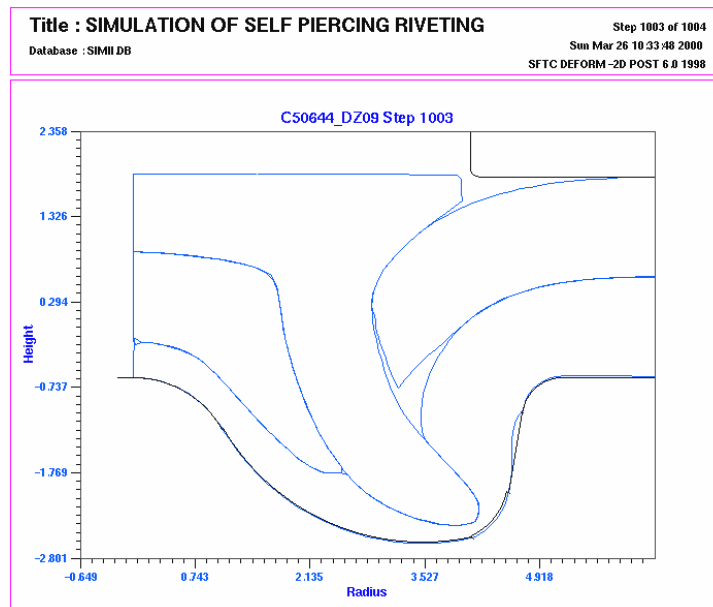


Figure 4.1. Image of rivet region, which is the base-model of the geometry. [5]

The total length of the specimen is 90 mm, and the height is 23.15 mm. The total width of the model is 45 mm but due to symmetry the specimen width becomes 22.5 mm. The rivet has a waist-diameter of 5 mm and a head-diameter of 7 mm. The sheets are 1.15 mm thick. The inner bending radius is 2 mm and the centre of the rivet is placed 13.15 mm from the lower side of the specimen. The measurements are chosen according to other reports on crash simulations at SIMR [6,7,8] and according to Volvo corporate standard (VCS 5601,029). For the final geometry model, see figure 4.2 and 4.3 for an overview.

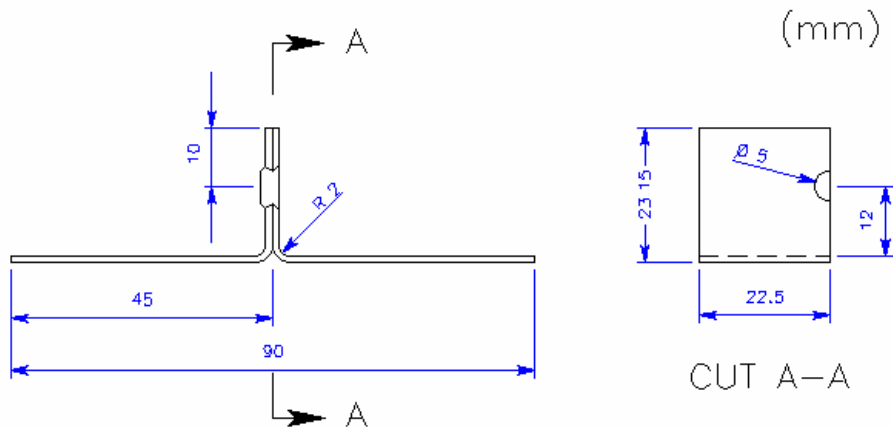


Figure 4.2. Geometry of model specimen. Sheet thickness is 1.15 mm.

The right sheet is referred as the top sheet or the right sheet in the report.

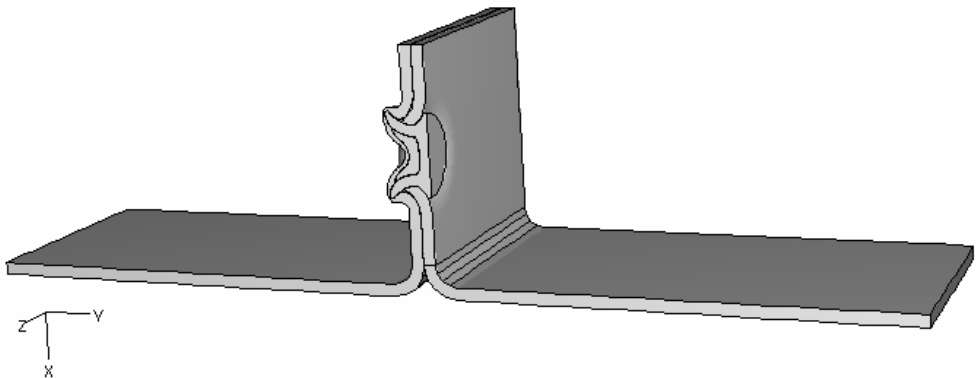


Figure 4.3. Overview of model.

4.1.2 Mesh

The mesh procedure is used to divide the model into small elements. The smaller these are the more accurate the simulation will be. The disadvantage with smaller elements is the time to calculate and the input file-size which both increases.

Different meshes were tested to find an optimal mesh density. The mesh in figure 4.4 and 4.5 was finally chosen, with enough elements to provide adequate precision in the

calculations. The mesh consists of 8642 elements to cover the whole model, with a higher density around the rivet region.

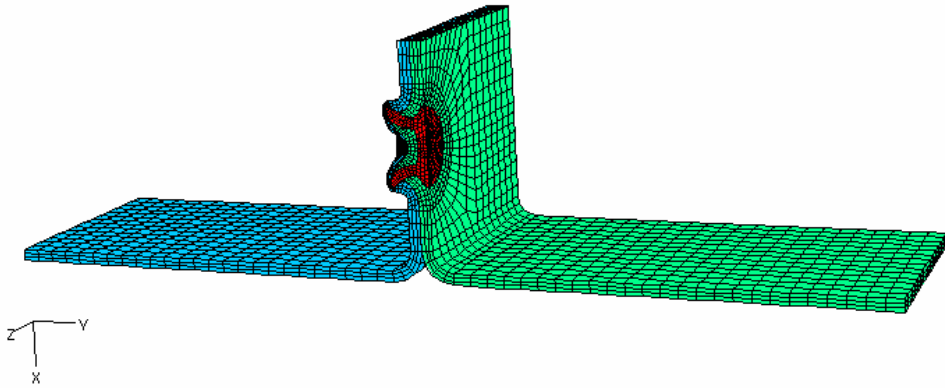


Figure 4.4. Mesh of the specimen.

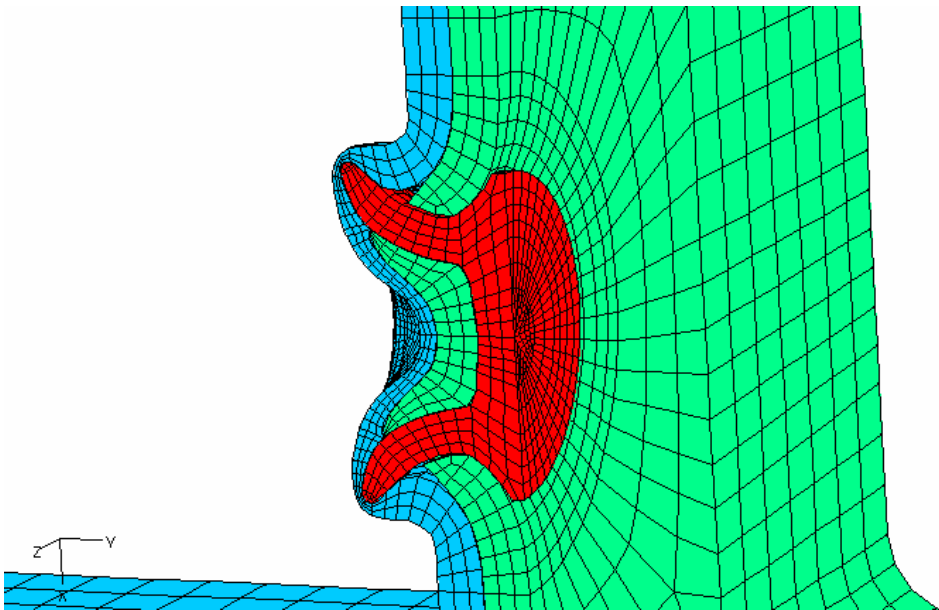


Figure 4.5. Mesh in close-up of rivet region.

Simulations of crash testing normally give large deformations, which can give distorted elements. When elements become distorted the calculation time increases due to the explicit procedure and in the worst case the calculation can be prevented. To minimize the distortion of elements there is a facility tool in ABAQUS named adaptive mesh [4]. This tool makes it possible to maintain a high-quality mesh throughout an analysis, even when large deformations occur, by allowing the mesh to move independently of the material and rebuilding the mesh in a defined area during the simulation. Adaptive mesh is not necessary in this investigation due to the relative small plastic strains. Another reason is that the deformation plots show no obvious distorted elements.

4.1.3 Choice of element

Experience from earlier work [7,8] shows that the most well suited type of element for these analyses is the solid element type C3D8R; a three-dimensional eight-node linear brick element with reduced integration and hourglass control. Eight-node element means that each element consists of 8 nodes as in figure 4.6. This element type gives 12246 nodes in the whole model.

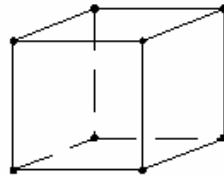


Figure 4.6. Eight-node brick element.

Reduced integration means that the order of integration is lower than that of full integration. The order of integration is here only one point in each element and this is placed in the centroid. This may result in spurious zero-energy modes that destroy the FE solution. Zero-energy modes means that in spite of the deformation of the element the integration point doesn't experience any strain, i.e. no energy is registered (see figure 4.7). If spurious zero-energy modes are not created, reduced integration may increase the accuracy of the FE solution, since it tends to soften the stiffness of the model [1]. Hourglass control is a control of these zero-energy modes.

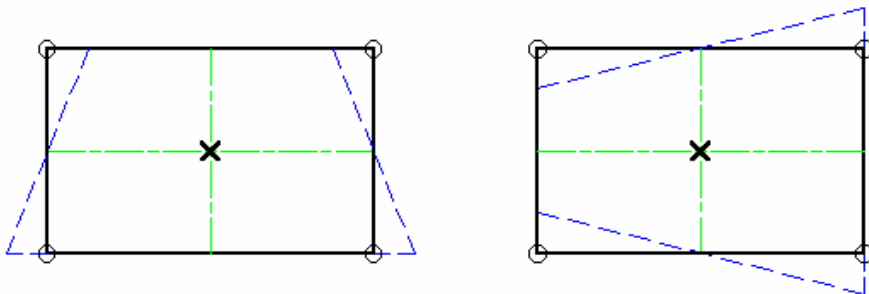


Figure 4.7. Elements showing a deformation (dashed line) but the integration point (cross) isn't moving.

4.1.4 Contact interaction

All surfaces, with potential contact, have been assigned contact interactions. The surfaces are shown in figure 4.8 with table (4.1) belonging to it.

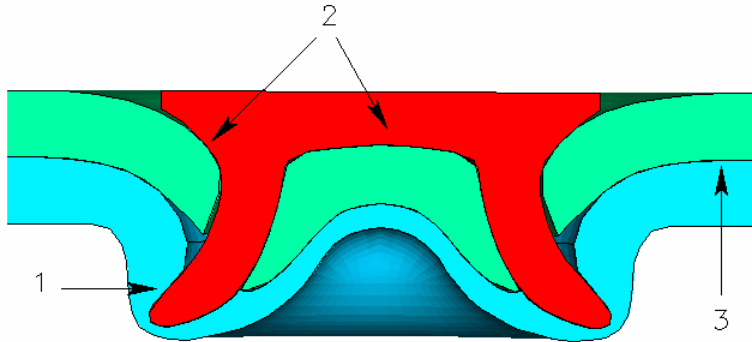


Figure 4.8. Close-up of rivet region showing different contact surfaces.

Table 4.1

Number	Master	Slave
1	Rivet	Bottom sheet
2	Rivet	Top sheet
3	Top sheet	Bottom sheet

The contact interaction is a so-called Master-Slave, which means that Master-nodes can penetrate a Slave-surface, but a Slave-node can't penetrate a Master-surface.

All contact surfaces have a initial clearance gap of 1 μm between each other, in order to simplify the calculation. The coefficient of friction (μ) was estimated to 0.2. This parameter will be investigated later in the report.

4.2 Material data

Two materials were used in the sheets;

- A deep drawing quality steel (DDQ), and
- A dual phase steel, with ultimate strength of 600 MPa (DP600).

The rivet material is a martensite boron steel.

These materials were used in earlier investigations of SPR and other joining methods at SIMR [6,7,8]. The materials were assumed to have an elasto-plastic response with the elastic parameters Young's modulus (E) of 210 GPa and a Poisson's ratio (ν) of 0.3. The materials are isotropic and have a mass density (ρ) of 7900 kg/m^3 which is assumed to correspond to steel. The mass of the simulated model, figure 4.3, is then about 27 g.

The Johnson-Cook plasticity model of ABAQUS/Explicit [4] was used to describe the plastic constitutive material behaviour and is described in chapter 3.4. The Johnson-Cook plastic and rate dependent parameters are shown in table 4.2 below.

To be able to use the Johnson-Cook plasticity model, some assumptions and estimations were done. A strain rate sensitivity (C) of 0.01 was used as a reference and in most of the simulations. Because of numerical reasons and to correspond with earlier work, done at SIMR [7,8], the material constant A will be equal to 1. This means that the initial yield strength is 1 MPa.

Table 4.2. Johnson-Cook parameters for the consisting materials.

Steel	A (MPa)	B (MPa)	n	C	$\dot{\epsilon}_0$ (s^{-1})
DDQ	1	550	0.25	0.01	0.001
DP600	1	1000	0.15	0.01	0.001
Rivet	1	2000	0.05	0.01	0.001

Figure 4.9 illustrates the true stress-true plastic strain curves for the rivet, DDQ and DP600 steel. Figure 4.10 shows a close-up on the DDQ and DP600 steels. Both figures represent the static part of the Johnson Cook model. Note that especially the failure strain of the rivet material is smaller than that appears in the figure. Both figures have just an illustrating purpose, to show the difference in strength between the steels.

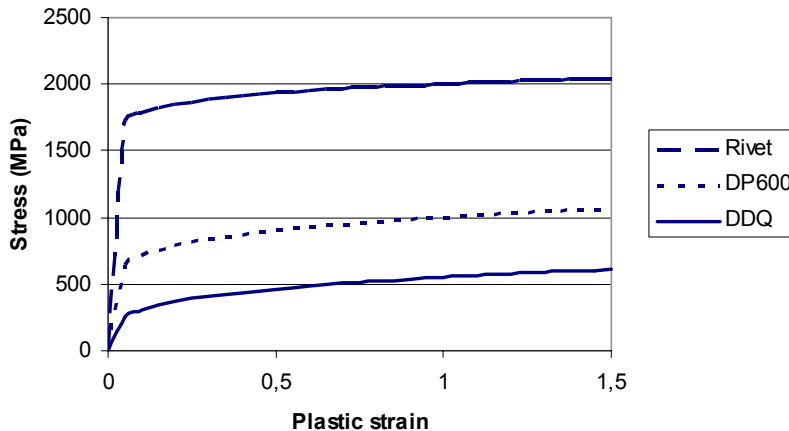


Figure 4.9. Stress-plastic strain diagram for the materials.

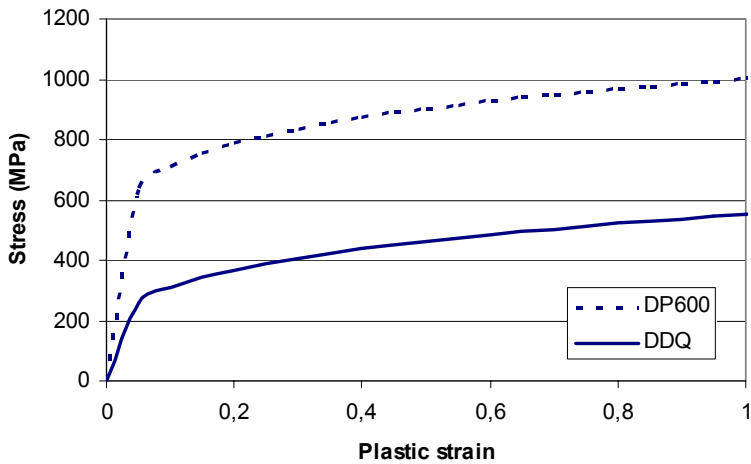


Figure 4.10. Stress-plastic strain diagram for the sheet materials.

The chosen material parameters result in $R_{p0,2}$ – values of 117, and 395 MPa for the DDQ and DP600 steel respectively.

4.3 Boundary conditions and loading

4.3.1 Boundary conditions

In figure 4.11 the boundaries are shown. The left-hand border surface is constrained in all directions. Along the symmetry plane all nodes are constrained in the Z-direction and the right-hand border surface is constrained in the X- and Z-direction. A table (4.3) is also presented to simplify the understanding. Constrained means that the displacement is prevented in a certain direction.

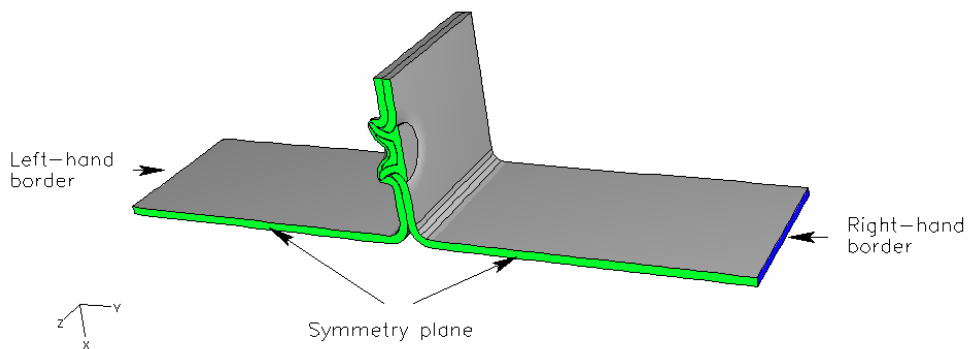


Figure 4.11. Explanation of the boundaries.

Table 4.3. Boundaries with zero-valued BC's.

	X	Y	Z
Left-hand border	✓	✓	✓
Symmetry plane			✓
Right-hand border	✓		✓

4.3.2 Loading

A constant velocity is applied in the Y-direction at the right-hand border surface, i.e. a pull load. See figure 4.12 below.

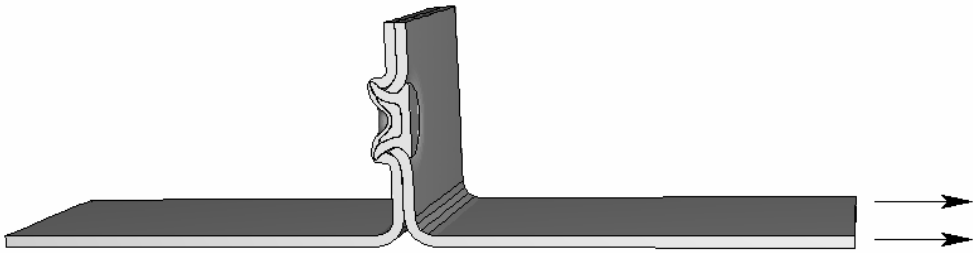


Figure 4.12. Velocity is applied at the right-hand border surface.

The velocity was applied in different ways by an amplitude code in ABAQUS [4]. The amplitude curves allow arbitrary time variation of load. Three different types of approaches (figure 4.12) were tested:

- Direct load, applied instantaneously at the beginning of the step, which is used in most of the simulations,
- Tabular step, which has a constant slope to the final velocity and
- Smooth step, which applies the load smoothly by a non-linear interpolation.

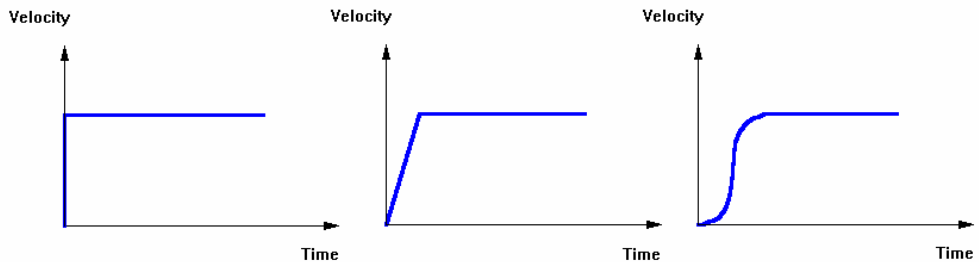


Figure 4.12. Direct load, tabular-step load and smooth-step load. The y-axis defines relative magnitude.

Simulations were done with 1, 10, 25 and 100 m/s (3.6, 36, 90 and 360 km/h), which are the amplitude velocities. There are no gravity forces involved in any of the simulations. A simulation with opposite load condition, i.e. pulling at the left-hand border, was done with similar results as for the right-hand load condition.

5. Results from FE simulation

In this chapter the influence of different parameters are evaluated and discussed. In table 5.1 and 5.2 a summary of the results from the simulations are shown. Due to oscillation of the curves it is not easy, in some cases, to see exactly where failure occurs. Failure is defined as the instant of complete separation of the parts in the model.

The loads reported were obtained by summation of the reaction forces at the right-hand border and combining these with the corresponding displacement. The results are multiplied by two to get the result for the whole model. This gives the load-displacement curves, from which the failure displacement, peak load and maximum load after oscillation are extracted.

To get the energy curves the load-displacement curves are integrated. The energy is then measured at failure displacement. Another option would be to let the program report the external work as a history output, which was done in some cases.

Table 5.1. Result information, with parameters according to chapter 4.

Velocity (m/s)	Material	Energy (Nm)	Failure displacement (m)	Peak load (N)	Max. load after oscillations (N)
1	DDQ	13.5	0.016	2130	1166
	DP600	29.3	0.0155	2377	2700
10	DDQ	18.0	0.018	9011	1198
	DP600	34.2	0.0165	19354	2697
25	DDQ	32.4	0.020	14721	1635
	DP600	49.7	0.018	30007	3620
100	DDQ	279.9	0.027	26502	*
	DP600	297.4	0.023	47331	*

* = Difficult to measure.

Table 5.2. Result information, the alteration is represented in the column "Parameter changed".

Velocity (m/s)	Material	Parameter changed	Energy (Nm)	Failure displ. (m)	Peak load (N)	Max. load after oscillations (N)
10	DDQ	$\mu = 0.0$	13.7	0.0155	9011	1052
		$\mu = 0.4$	21.1	0.020	9011	1322
		$C_{DDQ} = 0.05$	23.4	0.018	11431	1606
		$B_{rivet} = 1\text{GPa}$	18.4	0.019	9011	1197
		Reverse b.c.	17.6	0.018	9008	1208
		Tabular, λ	17.3	0.018	7144	1201
		Tabular, 3λ	17.4	0.018	3113	1218
		Smooth, λ	17.7	0.018	8506	1215
		Smooth, 3λ	17.3	0.018	4108	1211
		Length x 2	19.5	0.018	9310	1192
		Sym. x 2	17.8	0.0175	9801	1218
		Shear failure	16.9	0.0195	9008	1195
Double prec.	18.8	0.020	9008	1195		

5.1 Reference case

The reference case is chosen with respect to earlier work of finite element simulation of crash testing [6,7,8]. The reference case in this report is a self-piercing rivet peel specimen with a deep drawing quality sheet steel (DDQ). The velocity is 10 m/s and the coefficient of friction is 0.2. For other material data see chapter 4.2. No adaptive meshing and no shear failure criterion have been used.

5.1.1 Load

See figure 5.1 for load result. As the velocity is applied a large peak occurs due to the response of the specimen. This first and largest peak is the “Peak load” and approximately around 9 kN. The following peaks are reduced, due to damping and the oscillation stops. These oscillations are due to structural dynamic effects. The maximum load after oscillation is slightly above 1 kN. From the start to the top at 11 mm displacement, a separation process of the initially vertical legs is performed. After this and to the load drop at 18 mm, the right sheet is pulled over the rivet head as been shown in figure 5.2. A noticeable load drop shows the failure of the joint at approximately 18 mm.

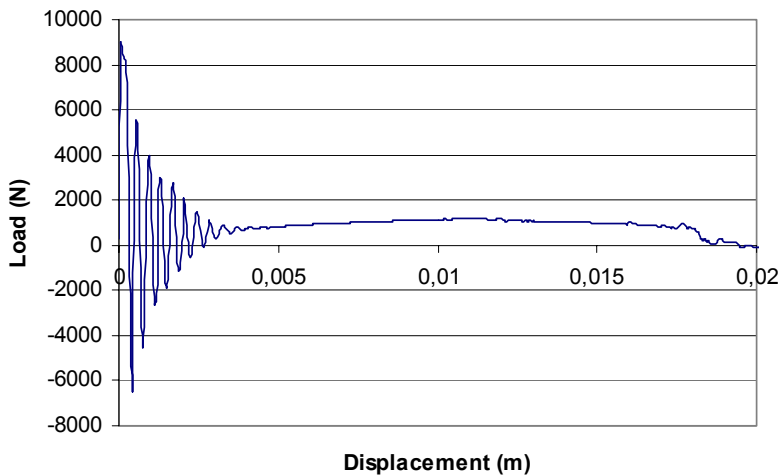
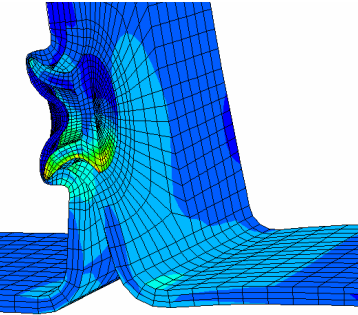
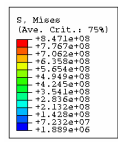


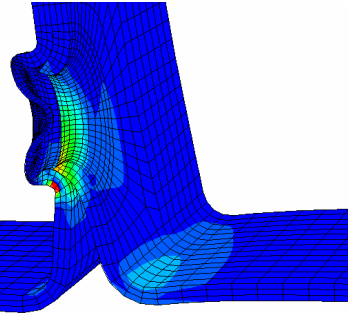
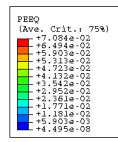
Figure 5.1. Load-displacement curve for the reference case.

The wavelength (λ), in the oscillations, is from this figure calculated to about 370 μm . This value is then transformed into time with the velocity of 10 m/s. The result is then 37 μs , which is used later in the report in load application, chapter 5.7.

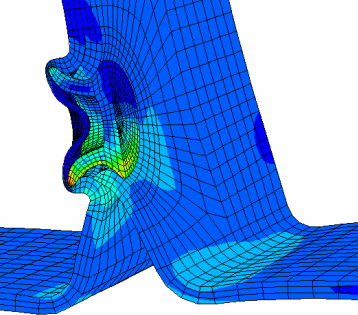
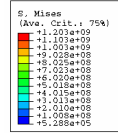
Figure 5.2 represents a number of plots from ABAQUS, showing the von Mises stress in Pascal [Pa] and the effective plastic strain [ϵ] (PEEQ), at different displacements. The joint is disintegrated by the top-sheet peeling itself over the rivet. For the von Mises cases the blank part is removed to get a better view of the rivet. The blank part takes practically no stress. In the PEEQ cases the rivet and blank are removed for a better view of the sheets, which are the mostly affected parts.



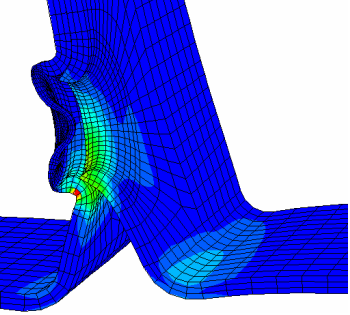
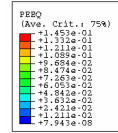
3 mm



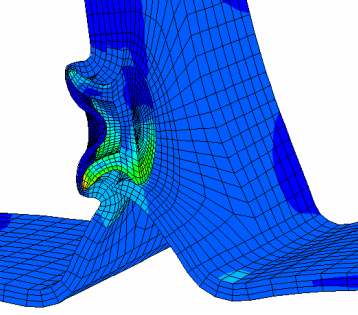
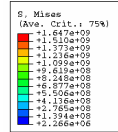
3 mm



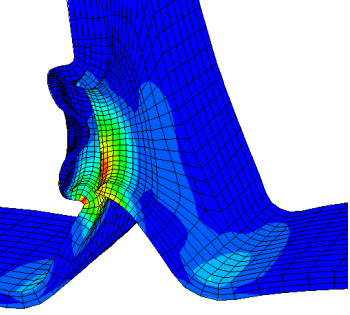
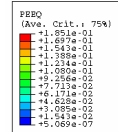
6 mm



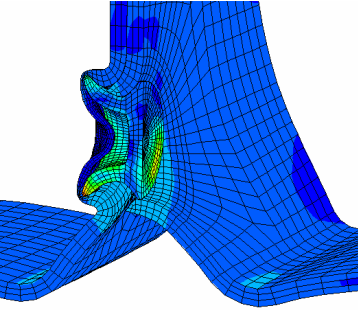
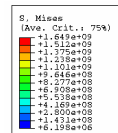
6 mm



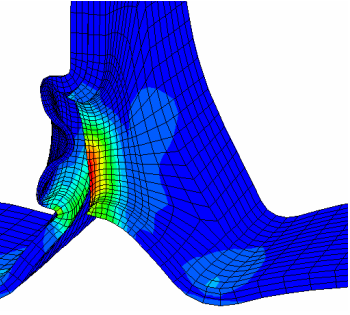
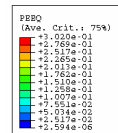
9 mm



9 mm



12 mm



12 mm

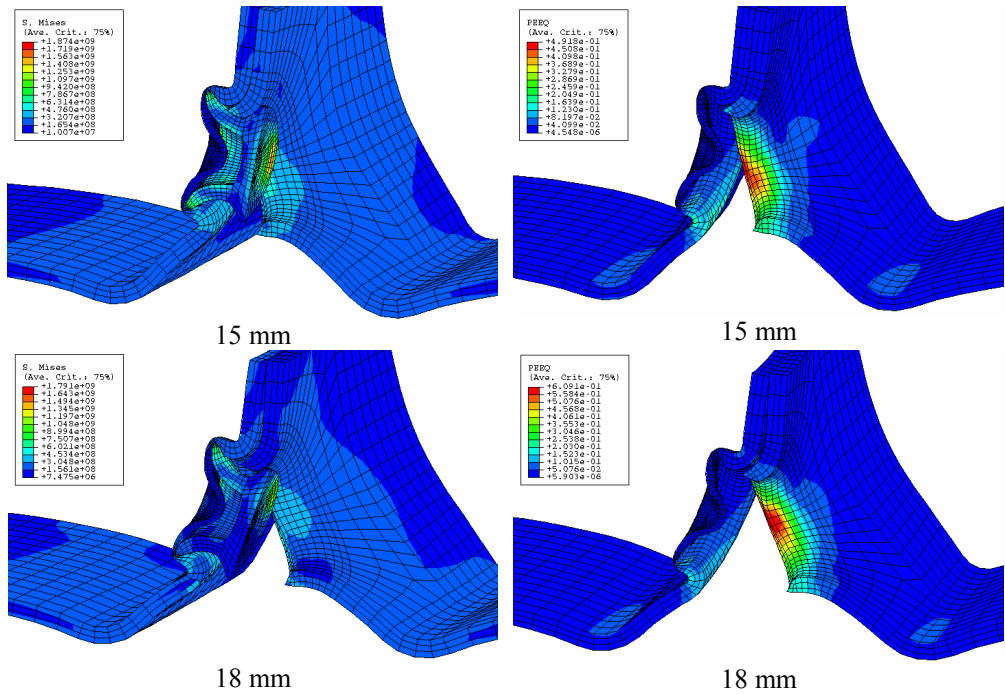


Figure 5.2. ABAQUS pictures. Mises equivalent stress [Pa] and equivalent plastic strain [ϵ] (PEEQ) at 3, 6, 9, 12, 15 and 18 mm of displacement. Some parts are removed for a better view.

5.1.2 Energy

The energy (total) in the model, which also can be named external work, is composed of different energies. The most interesting energies are shown below;

- ALLAE: “Artificial” strain energy associated with constraints used to remove singular modes (such as hourglass control),
- ALLFD: Total energy dissipated through frictional effects,
- ALLKE: Kinetic energy,
- ALLPD: Energy dissipated by rate-independent and rate-dependent plastic deformation and
- Other energies.

The energy magnitudes are shown in figure 5.3-5.6. The sum of these energies is represented in figure 5.7.

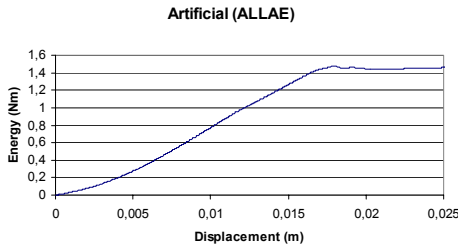


Figure 5.3. ALLAE, artificial energy.

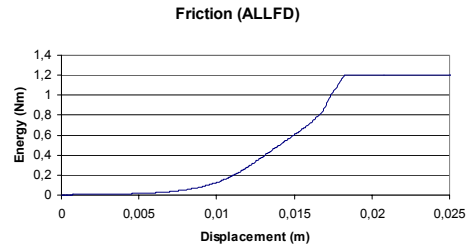


Figure 5.4. ALLFD, friction energy.

The artificial energy (unphysical) is about 10 % of the plastic energy, which is perhaps slightly more than recommended. It could however perhaps be lesser with a different mesh or if the hourglass stiffness is reduced. The frictional energy is small in the beginning and starts to rise quickly after about half of the failure displacement. When a plateau is reached failure has occurred.

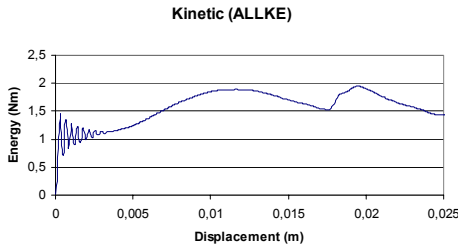


Figure 5.5. ALLKE, kinetic energy.

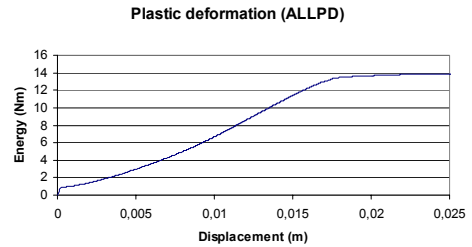


Figure 5.6. ALLPD, plastic deformation energy.

The kinetic energy curve shows a typical dynamic response result with the oscillating variations. After the failure there is still quite large kinetic energy variations due to the failure of the joint starting a secondary, transient, chock wave. For this case there are no other important energies.

The total energy is shown in figure 5.7 below.

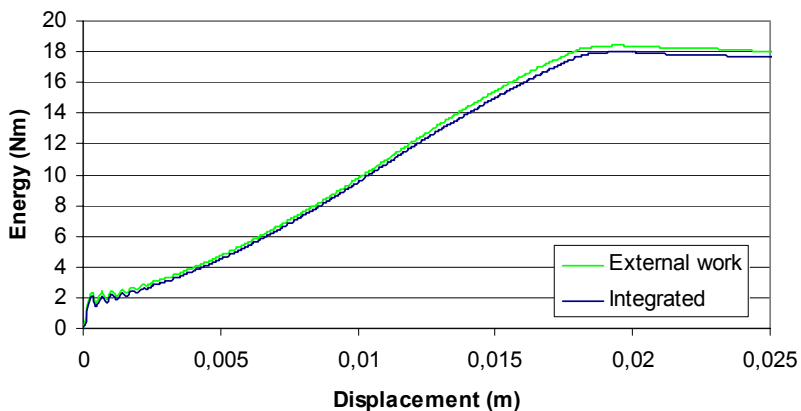


Figure 5.7. Energy-displacement curves for the reference case. Total energy as external work and integrated.

The external work is 1-2 % larger than the integrated energy due to rounding error and accuracy. The integrated value should be the most accurate.

As can be seen, the oscillations in figure 5.7 are due to the kinetic behaviour. The total energy mostly consists of the plastic deformation energy. When a plateau is reached, failure in the joint has occurred, i.e. no more energy is added to the model. When the energy curve drops, in the beginning, it indicates that the load has changed direction during the deformation lapse.

5.2 Influence of velocity

In this chapter different velocities are simulated. The applied velocity load is not equal to the velocity of the car. In fact in most cases the car velocity is much higher than the velocity that affects the joint, due to different kind of damping in the car structure.

Figure 5.8 illustrates how the loading rate velocity influences the load curve for the four simulated velocities with the DDQ steel. The load is measured at the same border were the velocities are, i.e. the right hand border.

The velocity has a significant influence on the structural dynamic response. One cause is that the material behaves differently as the strain rate changes with velocity.

The oscillations are dependent of the acceleration of the applied velocity load. As it is applied instantaneously it creates a very high acceleration, which starts a longitudinal transient chock wave. This wave propagates back and forth through the specimen. The damping in the model decreases the amplitude until the oscillating disappear.

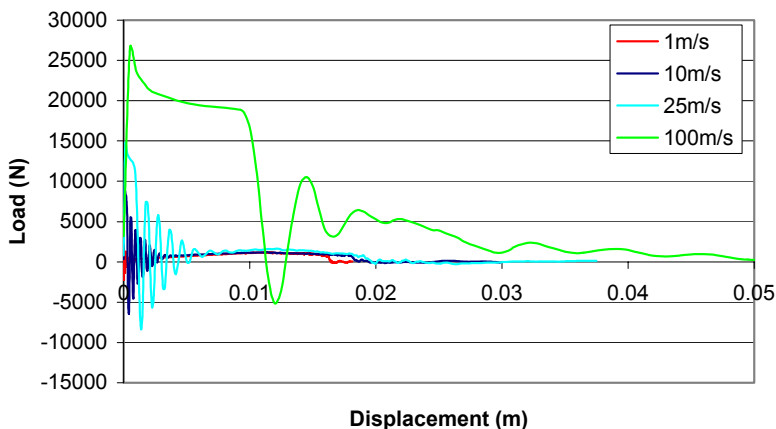


Figure 5.8. Load-displacement curves for different velocities with DDQ steel.

The load curve for the 100 m/s case shows a different behaviour compared to the other cases. A significant difference is that the load curve has a very long plateau and only a few peaks when oscillating. The failure process is extended and smooth, i.e. it is hard to see where failure occurs in the curve. Figure 5.9 shows an enlargement of the first 5 mm.

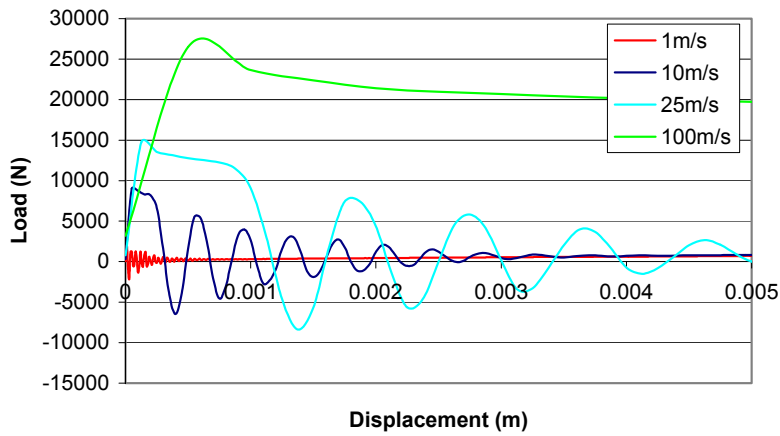


Figure 5.9. Load-displacement curves for different velocities with DDQ steel, close-up.

To be able to make a frequency analysis, the load curve was plotted against time. Figure 5.10 displays the result and shows that 1, 10 and 25 m/s has nearly the same frequencies. The frequency is about 27 kHz for the DDQ material. The 100 m/s plot has too few peaks to get a good estimation of the frequency.

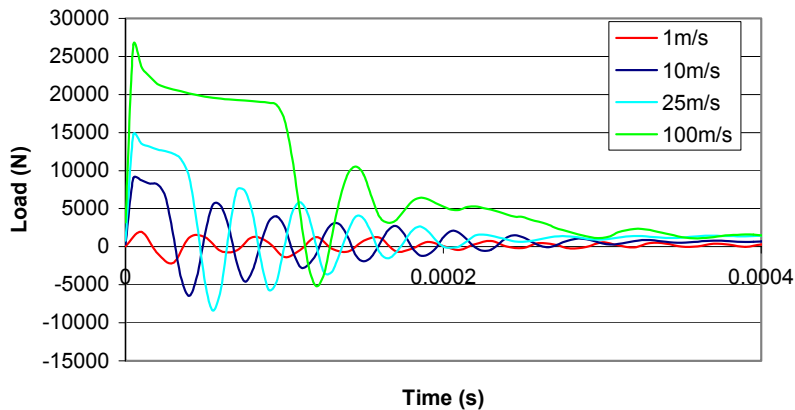


Figure 5.10. Load-time curves for different velocities with DDQ steel.

After the first peak, in the 10, 25 and 100 m/s cases, a kind of plateau is created. This plateau is explained later in this chapter.

Figure 5.11 shows the energy-displacement curve with all four velocities and DDQ material.

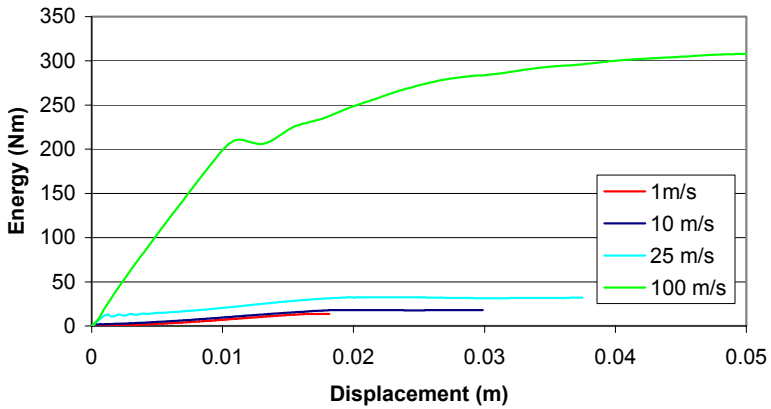


Figure 5.11. Energy-displacement curves for different velocities with DDQ steel.

The 100 m/s curve shows a strange behaviour with increase in energy after failure, which appears at 27 mm.

As explained earlier the energy consists of different kind of energies. A magnitude table is presented in table 5.3.

Table 5.3. Magnitudes of energy parts, measured at failure displacement. DDQ material.

Velocity (m/s)	ALLAE (%)	ALLFD (%)	ALLKE (%)	ALLPD (%)	OTHER (%)
1	9.8	6.8	0.2	82.5	0.7
10	8.5	6.2	9.6	75.7	0
25	5.2	4.0	30.5	60.3	0
100	1.6	1.1	53.1	44.2	0

The column “other” can also involve accuracy and rounding error.

Figure 5.12 shows deformed specimens at different velocities but with same displacements, except for the 1 m/s case that almost has the same displacement.

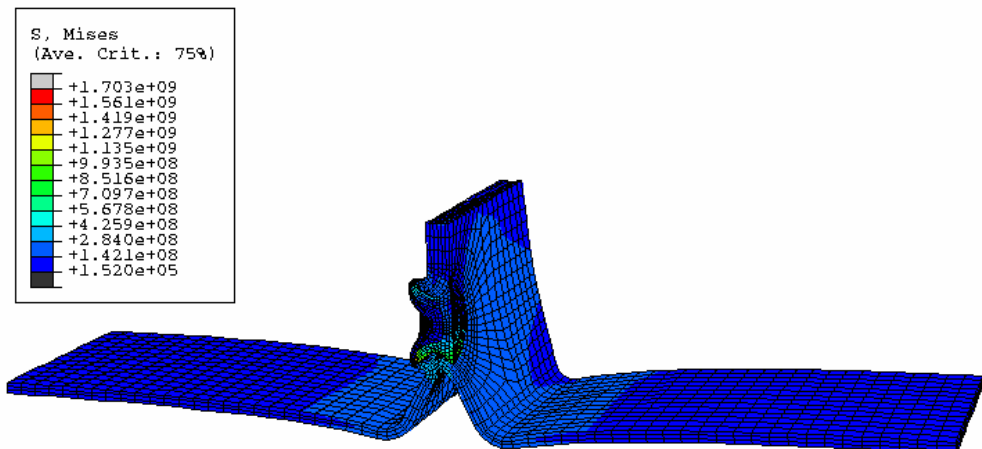


Figure 5.12a. 1 m/s with a displacement of 7.425 mm, DDQ.

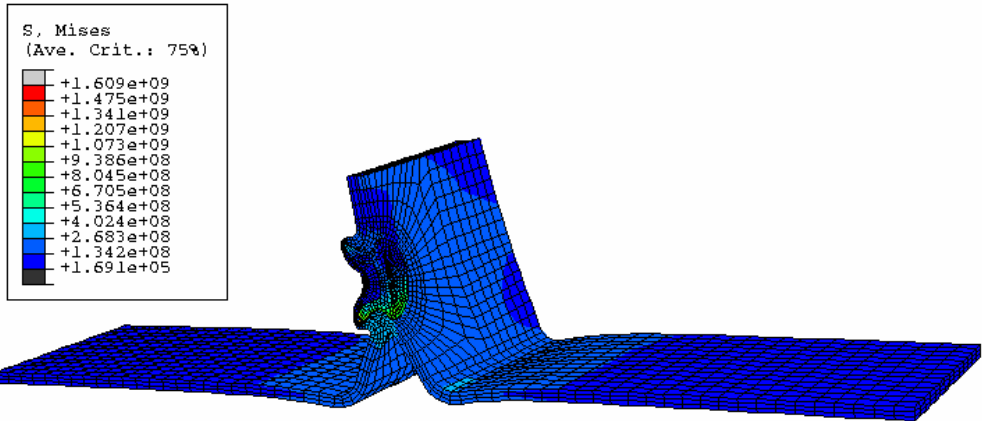


Figure 5.12b. 10 m/s with a displacement of 7.5 mm, DDQ.

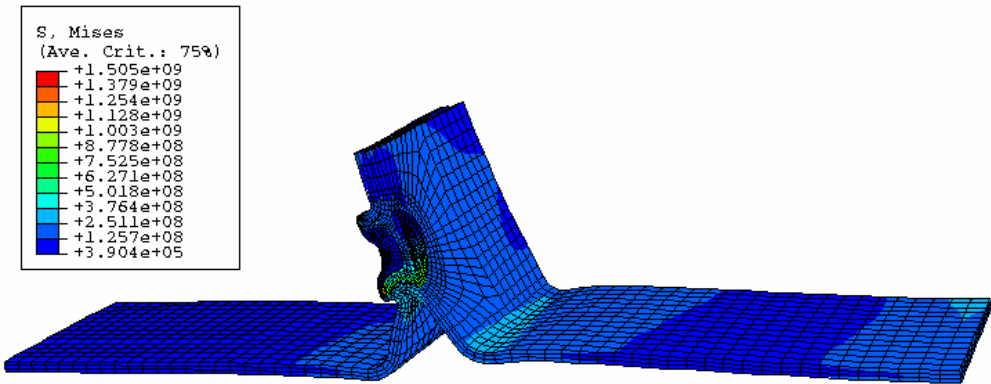


Figure 5.12c. 25 m/s with a displacement of 7.5 mm, DDQ.

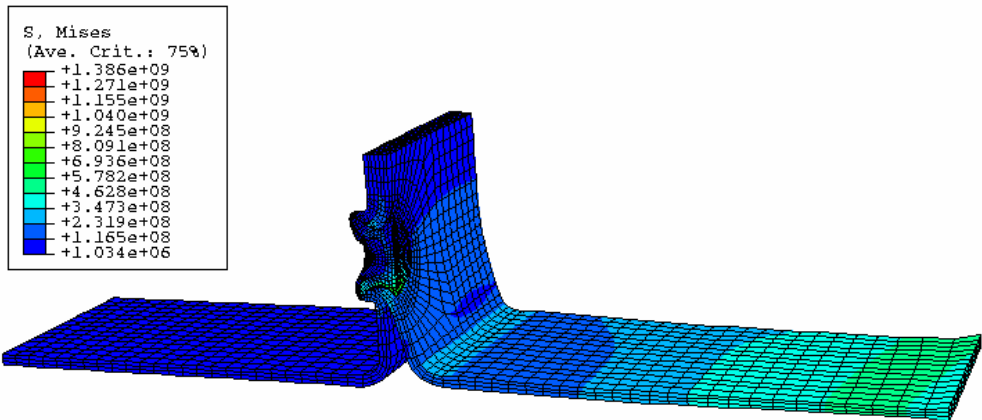


Figure 5.12d. 100 m/s with a displacement of 7.5 mm, DDQ.

It can be seen that the sheets take a quite symmetrical shape during deformation at 1 and 10 m/s. For the 100 m/s it is clear that the right hand sheet becomes deformed before the left-hand sheet. The 25 m/s case is somewhere in between the other cases.

In the 100 m/s case, necking has occurred close to the right-hand border. This is due to the very high deformation speed and the dilatational wave that doesn't reach the rivet region to transfer the plastic deformation. As the wave reaches the rivet region, the necking stops

and the deformation is concentrated to the rivet region. This is the explanation of the early plateau, after the first peak that is found in the load-displacement plots.

The dilatational wave is the same for all models. It is related to density, Young's modulus and Poisson ratio, which are the same in all simulations/models. The dilatational wave speed is calculated in another report [8], done at SIMR, to 6995 m/s.

Maximum stress (Von Mises) for all four velocities is shown in table 5.4, for both materials and with appertaining displacements. Total equivalent plastic strain (PEEQ) is also presented. The maximum stress appears in the rivet head close to the sheet and the highest value of PEEQ in the top sheet at the curvature that surrounds the rivet close to the rivet head, see figure 5.2.

Table 5.4. Maximum Von Mises stress and total equivalent plastic strain.

Material	Parameter	1 m/s	10 m/s	25 m/s	100 m/s
DDQ	Max. stress (MPa)	1865	1934	1936	2073
	Displacement (mm)	15.975	16.125	16.875	26.250
	Total PEEQ	0.58	0.61	0.60	0.83
DP600	Max. stress (MPa)	2164	2213	2230	2182
	Displacement (mm)	14.625	15.750	16.875	18.750
	Total PEEQ	0.45	0.46	0.45	0.63

The response for the DP600 steel is principally the same as for the DDQ steel. The curves for the DP600 steel are shown in figure 5.13 and an enlargement of the first 5 mm is shown in figure 5.14. The differences with DDQ are that the failure displacement is smaller and the loads are higher for the DP600 steel. This is the case for all velocities and more discussed later in the report.

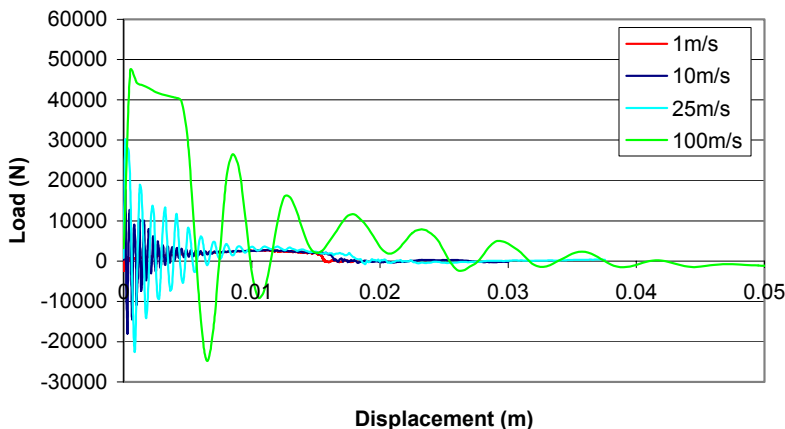


Figure 5.13. Load-displacement curves, different velocities and DP600 steel.

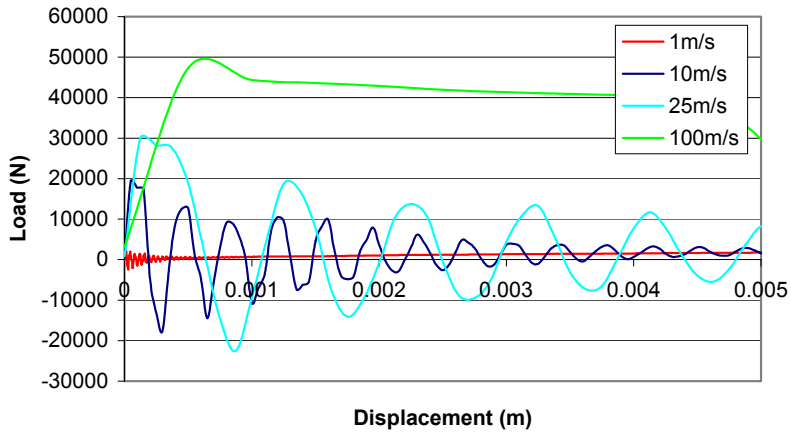


Figure 5.14. Load-displacement curves for different velocities with DP600 steel, close-up.

A frequency analysis is also made for the DP600 steel. A load-time curve is plotted below in figure 5.15.

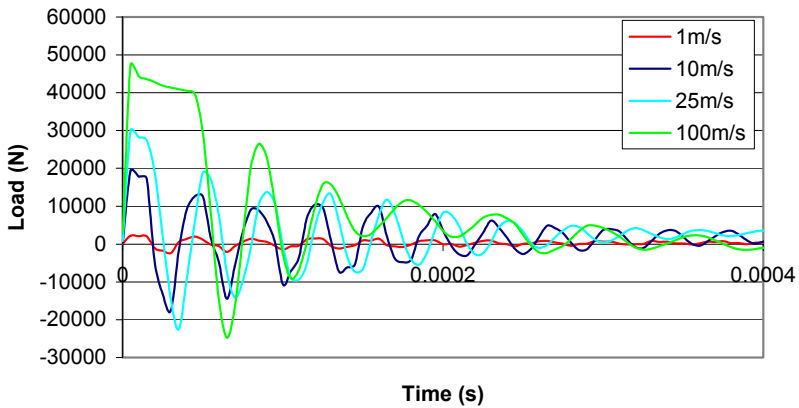


Figure 5.15. Load-time curves for different velocities with DP600 steel.

The frequencies in the DP600 case are calculated to 25-29 kHz. The 100 m/s case differs a little bit from the other cases.

The total energies for the different velocities are shown in figure 5.16.

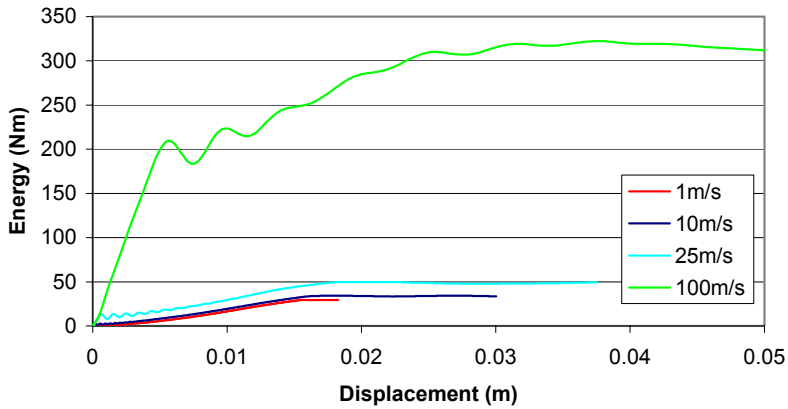


Figure 5.16. Energy-displacement curves, different velocities and DP600 steel.

A magnitude table (table 5.5) of the consisting energies is shown below.

Table 5.5. Magnitudes of energy parts, measured at failure displacement. DP600.

Velocity (m/s)	ALLAE (%)	ALLFD (%)	ALLKE (%)	ALLPD (%)	OTHER (%)
1	5.4	10.2	0.2	80.8	3.4
10	5.9	7.9	5.3	75.3	5.6
25	4.8	5.6	22.3	67.3	0
100	1.8	1.5	50.4	46.3	0

5.3 Influence of friction

To determine the influence of friction, the coefficient of friction (μ) was changed. Two other coefficients were tested besides the reference case (0.2); 0 and 0.4. The results can be seen in figure 5.17 and 5.18.

The load-displacement curve in figure 5.17 shows that the friction changes the failure displacement, where a higher coefficient gives larger failure displacement. This is due to the fact that more friction can hold the specimen together more efficient. The maximum load after oscillation increases slightly with higher coefficient.

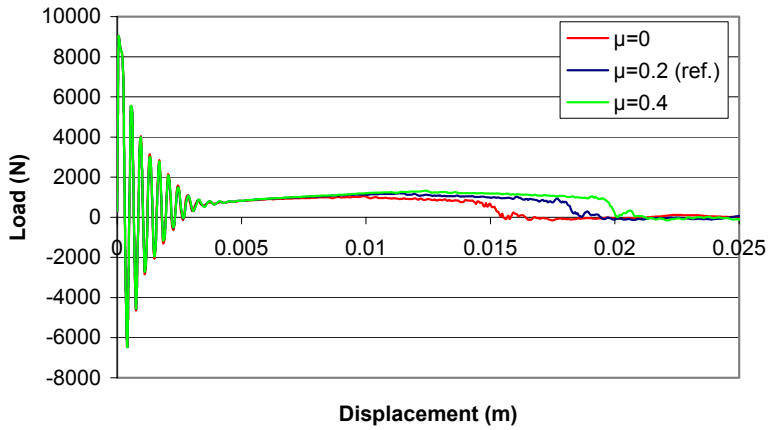


Figure 5.17. Load-displacement curves with different coefficient of friction. The velocity is 10 m/s and DDQ steel is used.

The PEEQ values increase with increased friction. For $\mu = 0, 0.2$ and 0.4 the PEEQ is $0.60, 0.61$ and 0.63 respectively.

The energy-displacement curve in figure 5.18 shows that the energy increases with higher coefficient of friction, because it's harder for the deformation process to proceed with higher friction. The change consists mostly of friction energy.

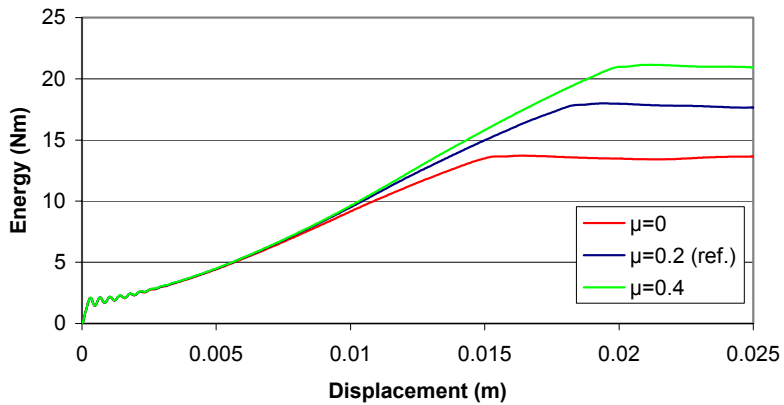


Figure 5.18. Energy-displacement curves with different coefficient of friction.

5.4 Influence of material

In this chapter the influence of changing some material parameters is investigated.

5.4.1 Comparison of the sheet steels DDQ and DP600

Figure 5.19 shows a comparison between load curves for the two different sheet materials. The velocity is 10 m/s and the material data is presented in chapter 4.2. DP600 shows a higher load level and a smaller failure displacement. The load level is more than twice as large for the DP600 material. This is due to the higher yield strength and strain hardening coefficient (B).

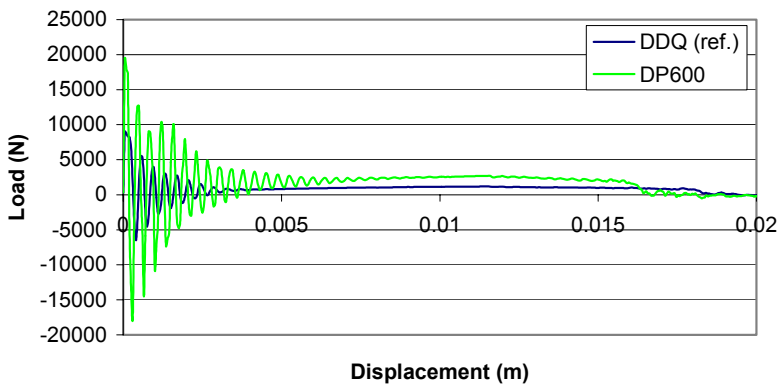


Figure 5.19. Load-displacement curves for DDQ and DP600 sheet steels at 10 m/s.

An energy plot is shown in Figure 5.20. The energy for the DP600 is almost twice as large as for the DDQ material. Most of the extra energy comes from the plastic deformation energy.

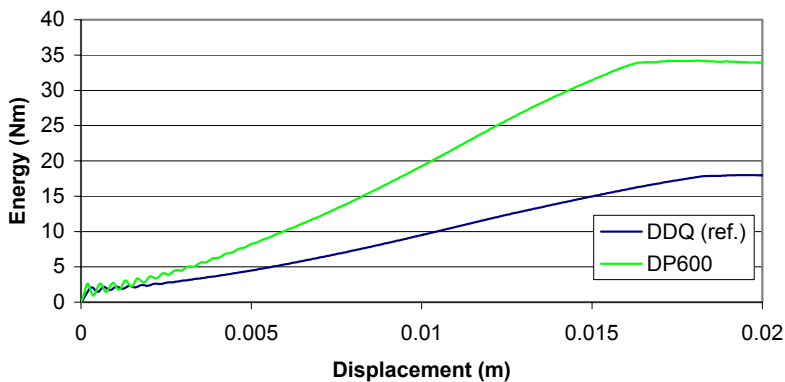


Figure 5.20. Energy-displacement curves for DDQ and DP600 sheet steels at 10 m/s.

Figure 5.21 shows the von Mises stress at equal displacements for the two different materials. The DP600 has higher stress in the model.

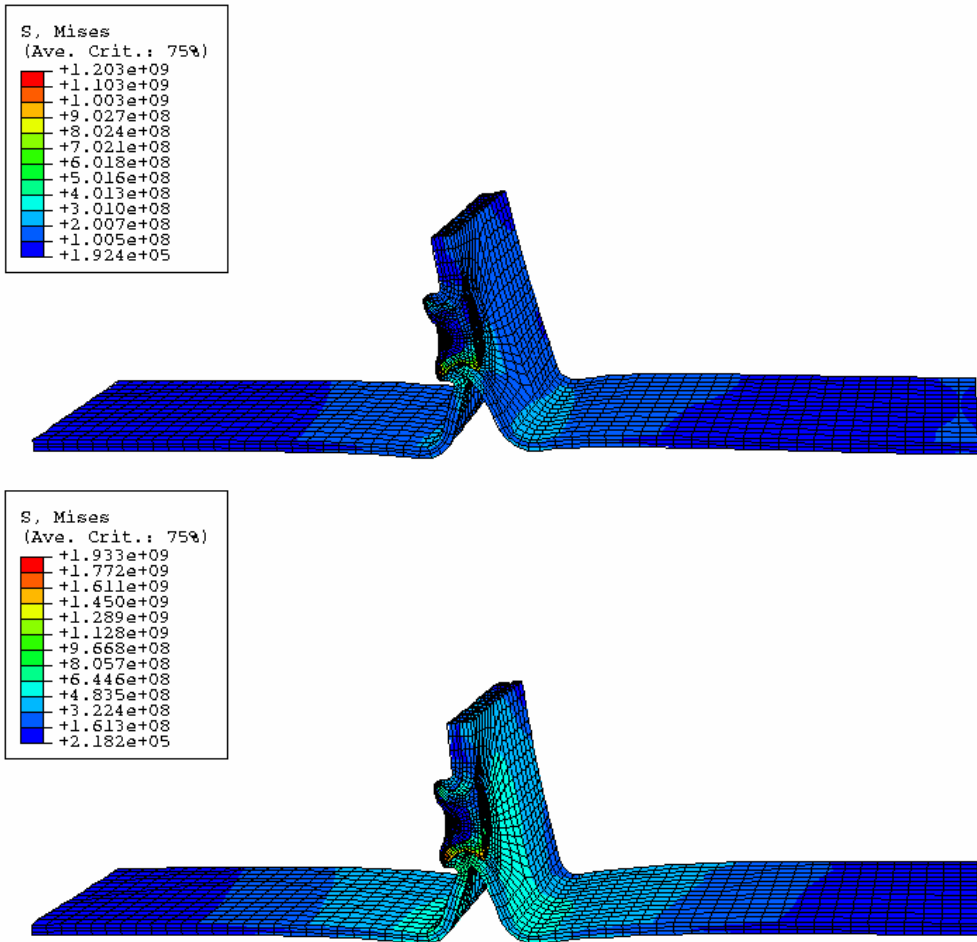


Figure 5.21. Von Mises stress [Pa] at 6 mm of displacement at 10 m/s. DDQ (top) and DP600 (bottom).

Figure 5.22 shows the same as figure 5.21 with the exception of the displacement, which is 12 mm instead of 6 mm. The result is the same.

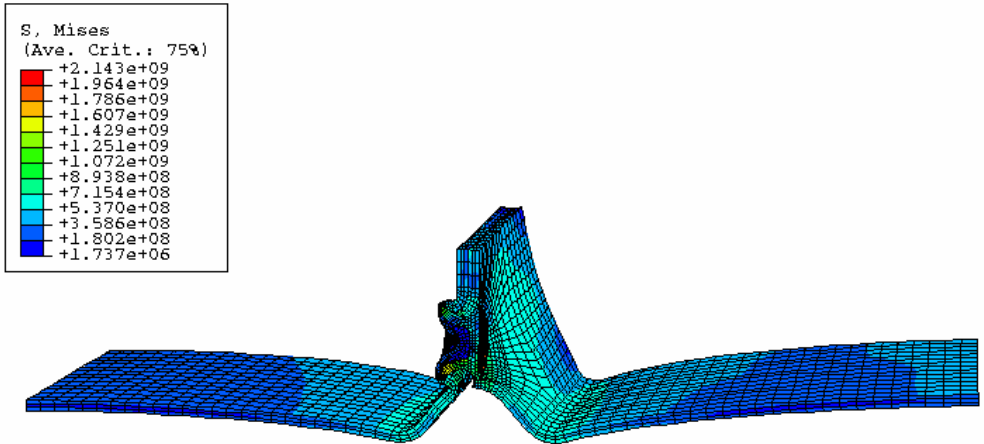
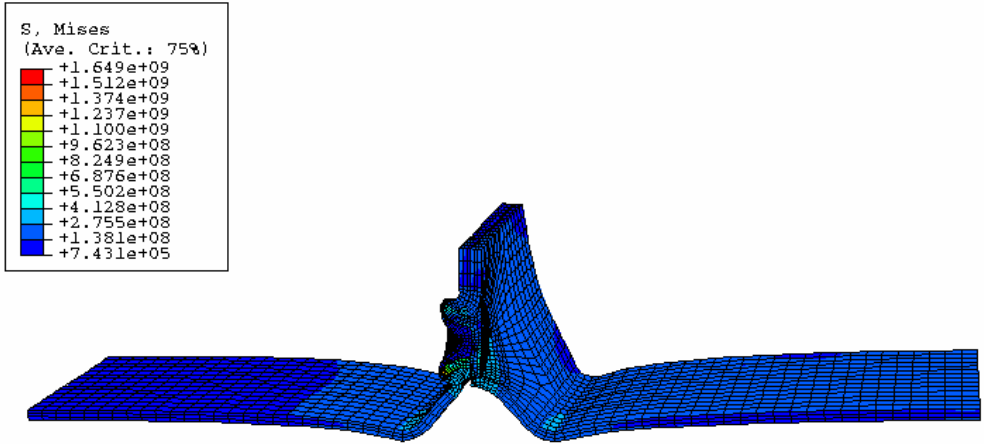


Figure 5.22. Von Mises stress [Pa] at 12 mm of displacement at 10 m/s. DDQ (top) and DP600 (bottom).

The maximum stress is presented in figure 5.23 for the DDQ steel and in figure 5.24 for the DP600. The maximum value, for DDQ steel, is found on the rivet on the other side of its head by the orange colour. For the DP600 steel, the maximum value is defined by the red colour on the rivet as shown.

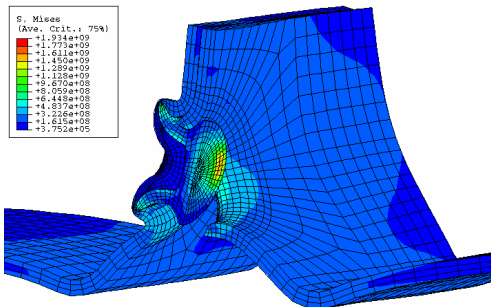


Figure 5.23. Von Mises stress [Pa] at 16.125 mm displ. Max value: 1.934 GPa. DDQ at 10 m/s.

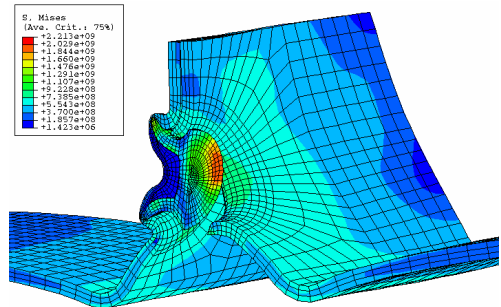


Figure 5.24. Von Mises stress [Pa] at 15.750 mm displ. Max value: 2.213 GPa. DP600 at 10 m/s.

5.4.2 Influence of strain rate sensitivity

The strain rate sensitivity is a parameter that influences the material when it's exposed to dynamic loads. Figure 5.25 illustrates how the load curve is influenced by the strain rate sensitivity of the reference steel DDQ at 10 m/s.

The load curve for the high strain rate sensitivity (0.05) shows a slightly higher load level, and a load drop that occurs a half-mm before the reference case.

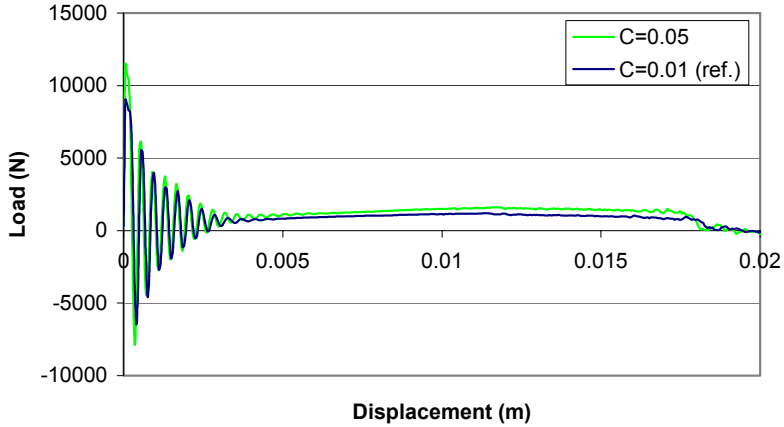


Figure 5.25. Load-displacement curves for different strain rate sensitivities.

The equivalent plastic strain (PEEQ) is slightly lower for the 0.05 case.

Due to higher load levels the energy of the 0.05 case becomes higher. The energy represented in figure 5.26 shows that a higher C-value gives higher energy.

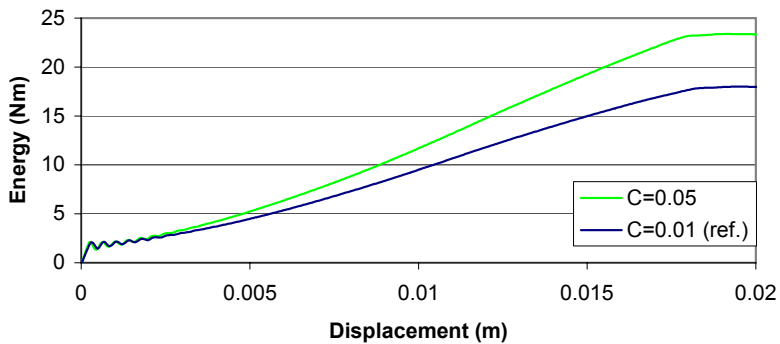


Figure 5.26. Energy-displacement curves for different strain rate sensitivities.

5.4.3 Influence of rivet strength

In this test the rivet strain hardening coefficient (B) was set to half of its original value, i.e. the parameter was set to 1000 MPa.

There was practically no different behaviour in the result curves. In the load curve the failure displacement was barely 1 mm longer for the 1000 MPa case, which makes the energy top-level value a little bit higher compared to the reference case. There is however a big change in the rivet. When the strain hardening coefficient is decreased to half, the von Mises stress decreases to approximately half. This has a significant effect on the PEEQ value, which increases from 0.05 to 0.43 (see figure 5.27)

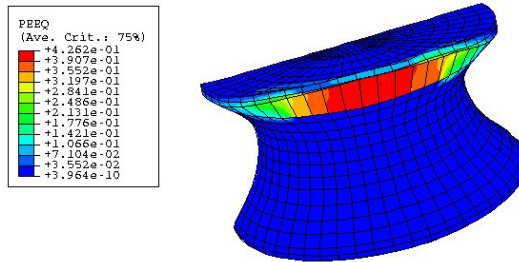


Figure 5.27. Rivet with $B=1000$ MPa. Maximum PEEQ.

5.5 Influence of cracking

In order to consider cracking, a shear failure criterion can be used in combination with the Johnson-Cook plasticity model. In ABAQUS/Explicit [4] it is possible to model/simulate a fracture process by giving an element a zero value of stiffness when a certain criterion has been reached at the corresponding integration point. The criterion is based on the value of the equivalent plastic strain (PEEQ). The maximum value of PEEQ in the reference case is 0.61. A value of $\epsilon_c=0.5$ was tested but with very similar result as the reference case. A smaller value was then tested. Figure 5.28 shows a load curve for the reference case when element deletion was activated at the effective plastic strain of $\epsilon_c=0.3$. This analysis was only successful when performed in double precision and is therefore also compared with a double precision reference case. The influence of solver precision is evaluated in chapter 5.9. An energy-displacement curve is shown in figure 5.29.

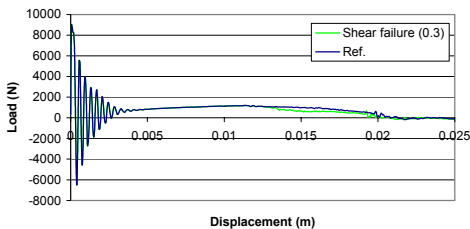


Figure 5.28. Load-displacement curve.

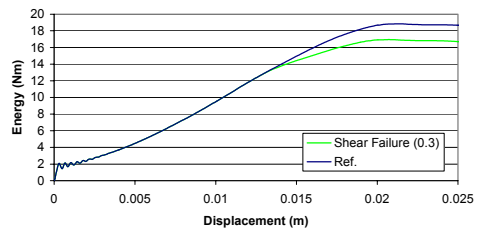


Figure 5.29. Energy-displacement curve.

Figure 5.28 shows that something happens at around 12.5 mm of displacement. The load drops due to a crack that appears in the top sheet. This crack is shown as the red, severely distorted elements in figure 5.30.

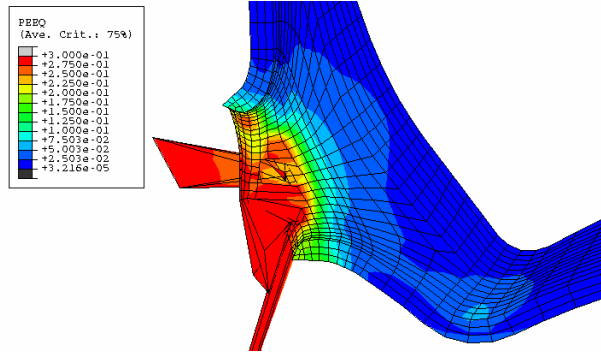


Figure 5.30. Shear failure criterion of 0.3. PEEQ.

5.6 Influence of specimen length

To investigate the influence of specimen length, the model was made twice as long. This means that the each sheet now is 90 mm instead of 45 mm.

As can be seen in figure 5.31 the oscillations have a longer duration as compared to the reference case, which is expected. The dilatational wave has a longer way to travel.

The maximum load and the failure displacement are about the same. Figure 5.32 shows that the energy levels are slightly higher for the long case.

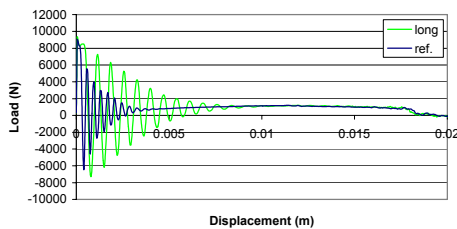


Figure 5.31. Load-displacement curve

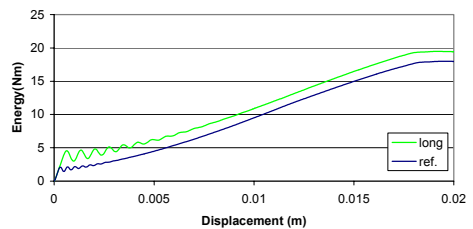


Figure 5.32. Energy-displacement curve

5.7 Influence of double symmetry

Double symmetry means that the same boundary condition that is put on the symmetry plane in figure 4.11 also is put on the opposite side. This corresponds to a multiple joint specimen, with rivets placed at 45 mm distance. Figure 5.33 and 5.34 show the load response and energy plotted against the displacement.

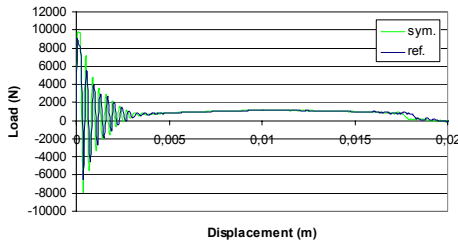


Figure 5.33. Load-displacement curve.

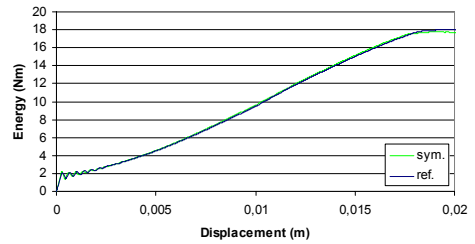


Figure 5.34. Energy-displacement curve.

As shown in figure 5.33 and 5.34 there is not much difference between the curves. The “double symmetry” has a shorter failure displacement, which contributes to the decreased energy. Maximum stress occurs at 16.5 mm with 1947 MPa and the PEEQ is the same as the reference case.

5.8 Influence of load application

To investigate the response of a different load application, two other applications were tested in addition to the direct approach. These two are the tabular and the smooth approach, which are investigated below. These kinds of load applications could be more realistic, than the direct approach, in a car crash.

5.8.1 Tabular

This approach is ramped from zero to the maximum velocity with a straight line, see figure 4.12. The time between zero and max velocity was set to be equal to the time for one and three wavelength, λ and 3λ . The time of one wavelength is evaluated in chapter 5.1.1 and has a value of $37 \mu\text{s}$.

The results are shown in figure 5.35-5.38. The main change is that the amplitude of the oscillations decreases in the load-displacement curves, which means that the peak load becomes lesser. Other results are similar to the reference case, which can be seen in figures 5.43 and 5.44.

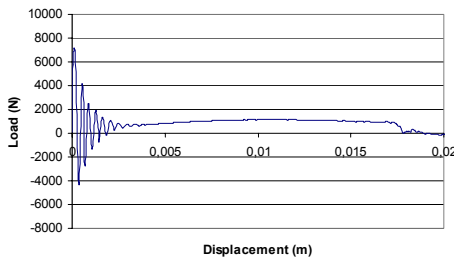


Figure 5.35. Tabular load application. Time step λ .

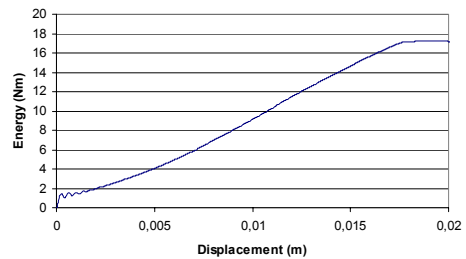


Figure 5.36. Tabular load application. Time step λ .

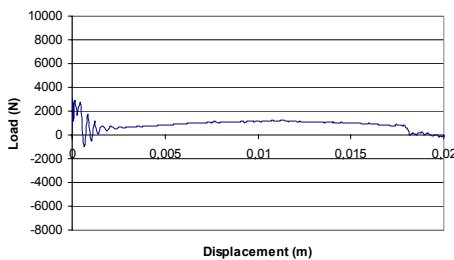


Figure 5.37. Tabular load application. Time step 3λ .

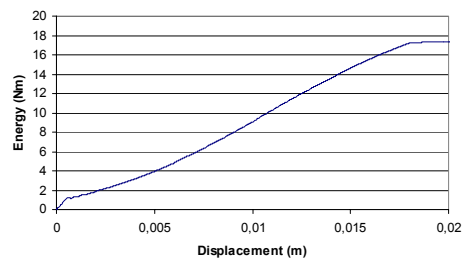


Figure 5.38. Tabular load application. Time step 3λ .

5.8.2 Smooth

Here the load is ramped with a function, a non-linear interpolation, with the goal to smooth the load application. The result is about the same as for the tabular case. The results are presented in figure 5.39-5.42.

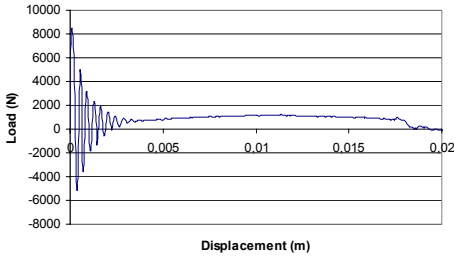


Figure 5.39. Smooth load application. Time step λ . Load-displacement curve.

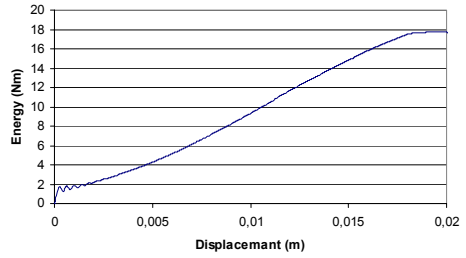


Figure 5.40. Smooth load application. Time step λ . Energy-displacement curve.

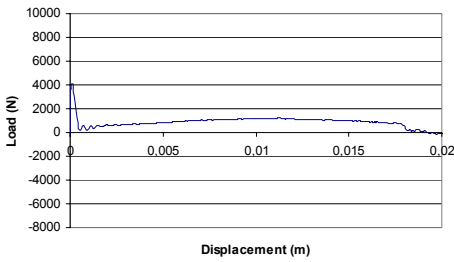


Figure 5.41. Smooth load application. Time step 3λ .

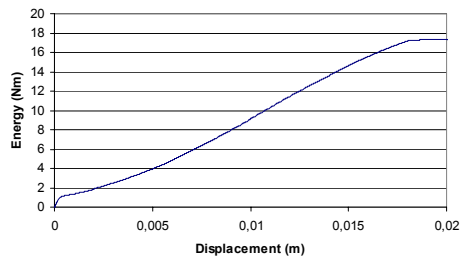


Figure 5.42. Smooth load application. Time step 3λ .

With the smooth approach, and a time step of 3λ , the oscillations almost disappear.

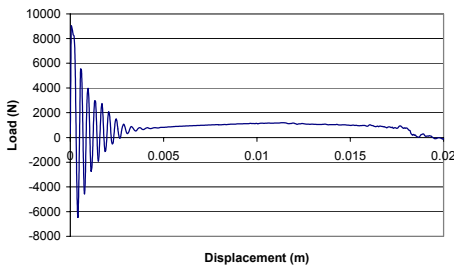


Figure 5.43. Load-displacement curve, ref. case.

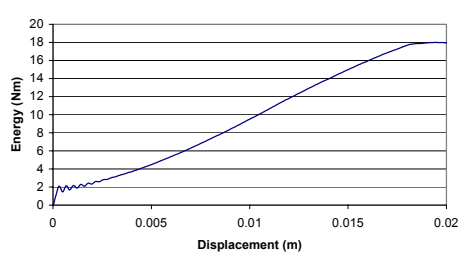


Figure 5.44. Energy-displacement curve, ref. case.

5.9 Influence of solver precision

In ABAQUS it is possible to choose between single or double precision in the solver. The single precision is faster but sometimes less accurate. Lesser accuracy can be of importance for simulations involving a large number of increments. The status file (.sta) makes a warning like: “The analysis may need a large number of increments (more than 300000), and it may be affected by round-off errors. It is recommended to run the job in double precision”. In this report there is one parameter that gives more than 300000 increments and a warning, when simulating at 1 m/s. The figures (5.45 and 5.46) show the different results with single or double precision.

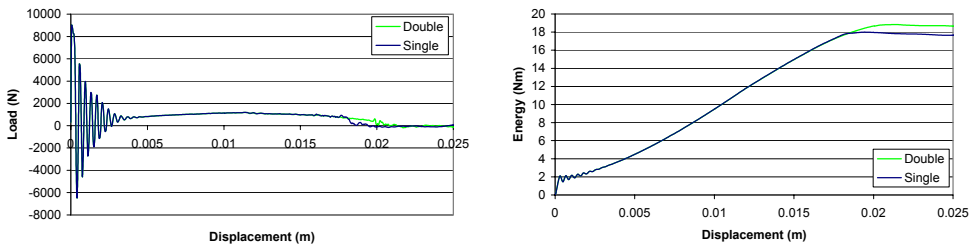


Figure 5.45. Single and double precision at 10 m/s with DDQ steel. Load and energy.

The result is exactly the same until the point of failure displacement. The double precision gives 2 mm longer displacement, which contributes to the increased energy at the end. The double precision gives the model a smoother failure process.

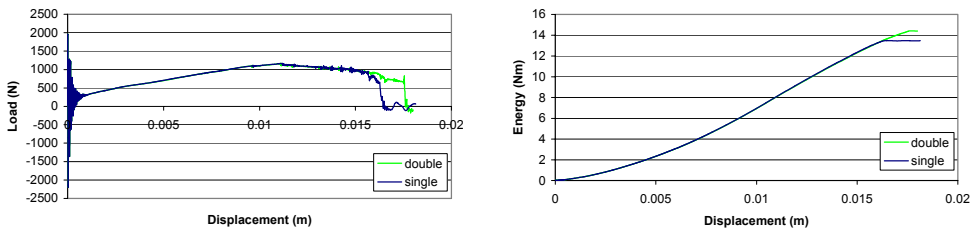


Figure 5.46. Single and double precision at 1 m/s with DDQ steel. Load and energy.

The 1 m/s case shows the about same result as for the 10 m/s case, except that here it is 1-1.5 mm longer failure displacement and that the load drop is more direct.

With the DP600 at 1 m/s, single and double precision gave practically the same result all the way.

6. Comparison with other joints

This chapter shows a comparison with spot- and laser-welded joints and some static tests. The main difference between the rivet joint and the spot- and laser welded joints is the failure process. In the rivet case the parts separate due to some plastic deformation. For the welded cases it is due to a large plastic deformation which contributes to necking and cracks.

6.1 Comparison with spot welded joints

Below are reported results by N. Saleh [7], who performed similar simulations on a spot welded specimen. Table 6.1 shows some of the results and figure 6.1 shows the geometry and mesh.

Table 6.1. Results on the spot-welded case.

Velocity (m/s)	Material	Energy (Nm)	Failure displ. (mm)	Peak load (N)
1	DDQ	29.2	23.5	2400
	DP600	52	23.0	4200
10	DDQ	33	25.1	6940
	DP600	57	24.2	15000
25	DDQ	45	27.2	12000
	DP600	67	25.1	25800
100	DDQ	258	30.9	19340
	DP600	270	25.0	40000

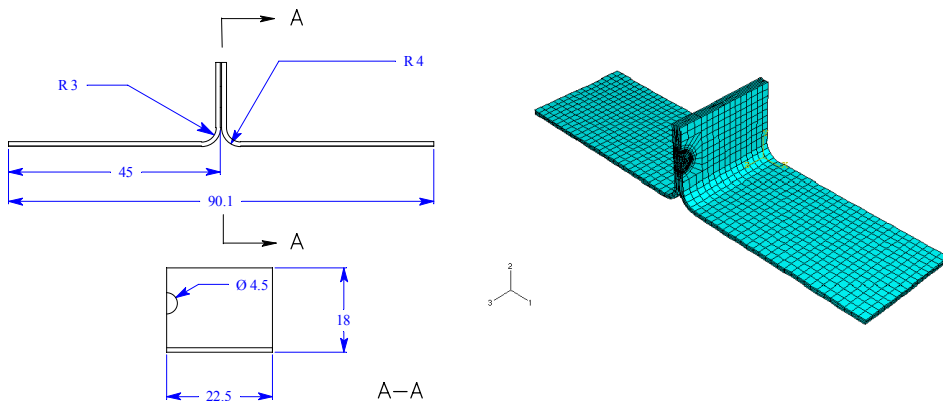


Figure 6.1. Geometry of the spot-welded case. Sheet thickness is 1 mm.

As shown in table 6.1 the energy, except for the 100 m/s case, and failure displacement is larger for the spot welded case, see table 5.1 for comparison. The peak load however is only larger for the 1 m/s case. The higher energy values on 1, 10 and 25 m/s may be due to higher plastic energy. For load comparison, with the DDQ sheet-steel, see figure 6.2 and 6.3.

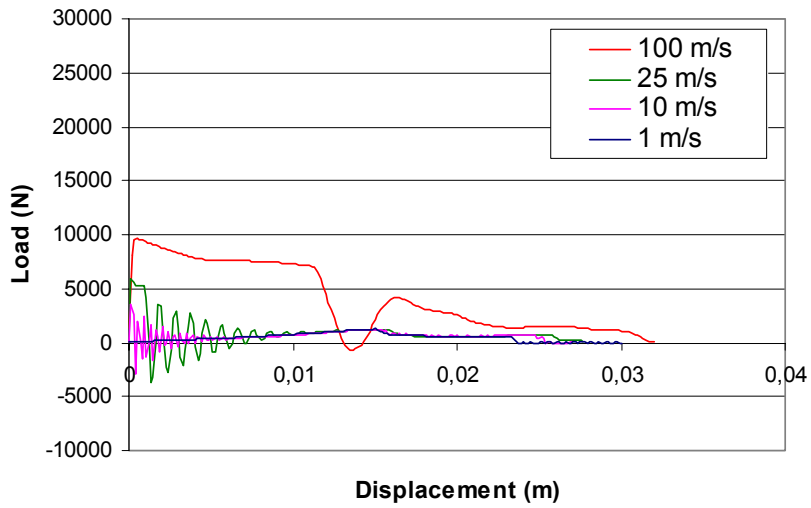


Figure 6.2. Load-displacement curves, spot-weld. This plot shows half of the load-amplitude. Multiply with two to compare with figure 6.3.

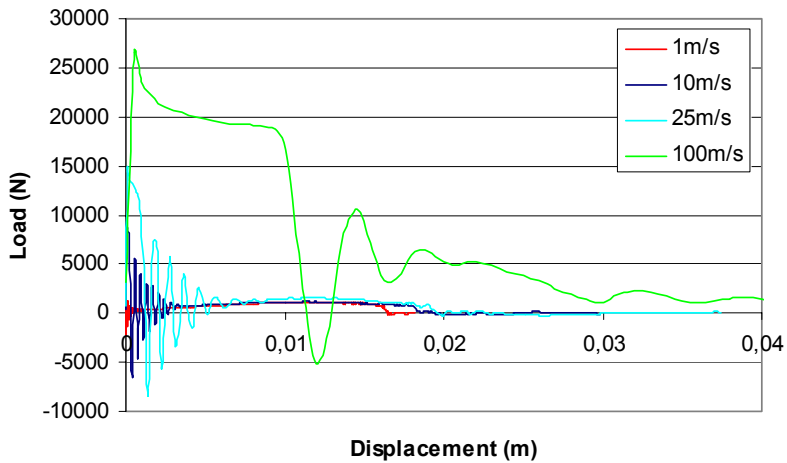


Figure 6.3. Load-displacement curves, SPR.

The behaviour of the curves is the same as for the SPR, except for the oscillating amplitudes, which are higher for the SPR case.

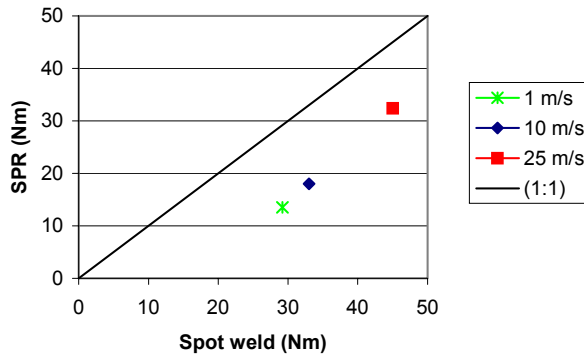
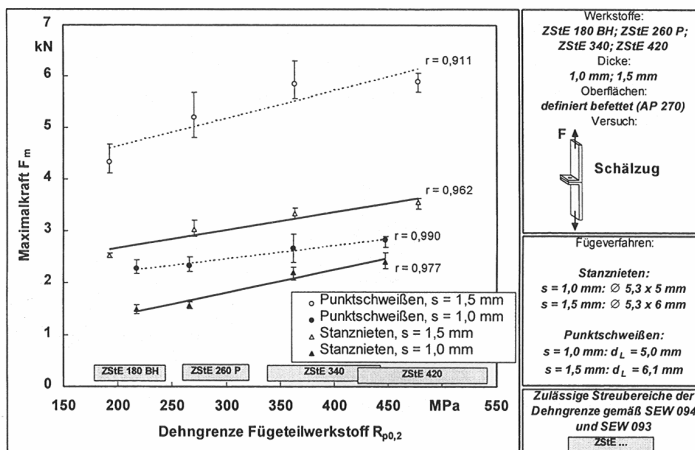


Figure 6.4. Comparison with maximum energy values.

In figure 6.4 an energy comparison is made. It shows that the spot-welded joint demands more energy. This is due to the fact that the spot-welded case has a quite large plastic deformation. The PEEQ shows a value above 1.5 in the 10 m/s case compared to 0.61 in the SPR case.

Figures 6.5 and 6.6 are taken from reference [11] and show static tests of spot-welds (Punktschweißen) and self-pierced rivets (Stanznieten). The results in figure 6.5 are compared with the 1 m/s simulation, from the present report. Figure 6.6 can not be compared with the results of the present report due to lack of the geometry dimensions of the German model. It shows however some differences in spot-welded and SPR joints.

Figure 6.5 shows curves related to maximum loads and $R_{p0,2}$. If considering the results from the 1 m/s cases, they agree with the static test.



Comparing data:
1 m/s case
 $s = 1.15 \text{ mm}$

DDQ
 $R_{p0,2} = 117 \text{ MPa}$
 $F_m = 1.2 \text{ kN}$

DP600
 $R_{p0,2} = 395 \text{ MPa}$
 $F_m = 2.7 \text{ kN}$

Figure 6.5. Static test of joints. s = sheet thickness.

A comparison shows that the 1 m/s case is 14 % lower with DDQ and 4 % higher with DP600. See table 6.2.

Table 6.2. Comparing results from figure 6.5.

Material	$R_{p0.2}$ (MPa)	Maximalkraft (kN)	Maximum load, present report (kN)
DDQ	117	1.4	1.2
DP600	395	2.6	2.7

Figure 6.6 shows load-displacement curves for two different materials and joining methods. The oscillations do not occur, due to the non-dynamic process. This figure shows the differences between SPR- and spot-welded joints. It can not be compared to the results of this report due to different geometry.

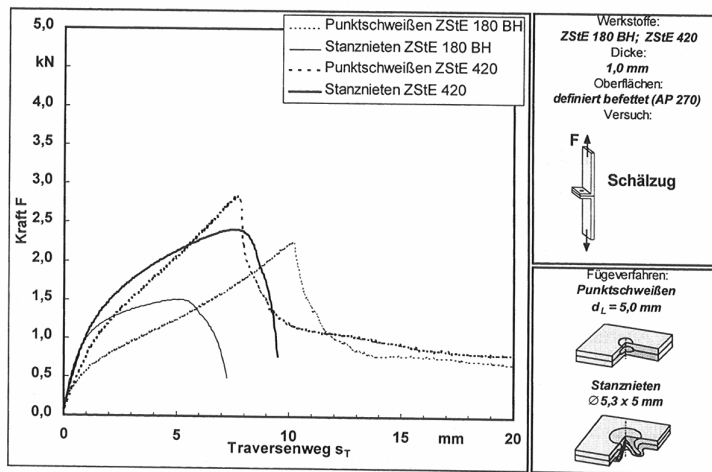


Figure 6.6. Load-displacement curves for spot welds and SPR. Thickness = 1.0 mm.

6.2 Comparison with laser welded joints

A. Melander has done a simulation on laser welded specimen [6]. Some of the results are represented below in figures 6.8 and 6.9. The geometry is the same as for the spot welded case and the laser weld runs through the entire width of the specimen. Maximum load, for a 10 m/s case with DDQ material, is around 18 kN. To compare with the SPR case, two figures (6.10 and 6.11) are presented.

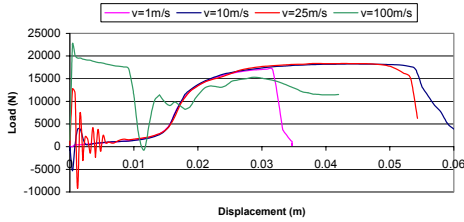


Figure 6.8. Load-displacement curves with all four velocities. Laser weld [6]. DDQ.

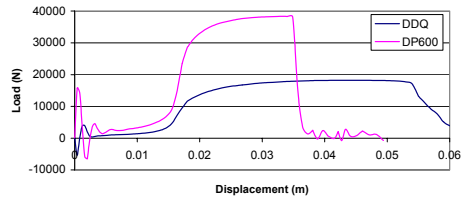


Figure 6.9. Load-displacement curves. Comparison of DDQ and DP600 material. Laser weld [6].

As the figures show, the failure displacement is quite long. The strong joint makes the initially vertical legs, below the weld, to straighten out totally. Failure occurs then dependent on the velocity as necking.

The main difference between the laser-weld and SPR cases is the loads after oscillations. In the laser case the load increases slowly due to separation of the legs. The load starts to rise rapidly when the specimen is straightened out and the sheets are elongated. The load drops as necking occurs. The big difference is therefore the plastic deformation, which is very high for the laser case.

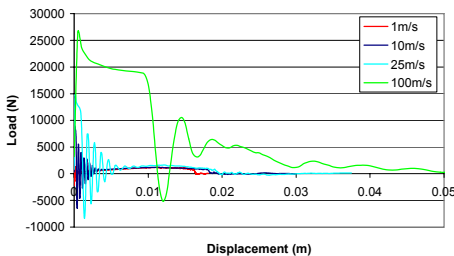


Figure 6.10. Load-displacement curves, SPR. DDQ.

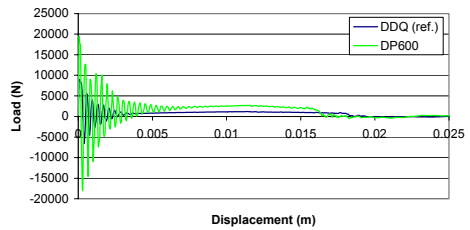


Figure 6.11. Load-displacement curves, SPR.

7. Conclusions

It was found that:

1. When making a finite element model, a number of parameters can be changed or introduced. This makes it time-consuming and difficult to get the most suitable model.
2. All the cases studied shows a model deformation process with the top (right-hand) sheet peeling itself over the rivet head and cause by that a failure in the model.
3. Higher velocity results in higher load levels, higher energy and therefore also larger failure displacement.
4. The DDQ steel showed lower load levels and larger failure displacement than the DP600 steel at all four velocity loads.
5. The deformation process was more or less similar at 1, 10 and 25 m/s. For these cases the rivet and the bottom sheet around it is quite still. For the 100 m/s case the rivet is a little bit drawn out from the bottom sheet and there is necking in the sheet nearby the right-hand border.
6. Direct application of the velocity load gives very large peak loads, which isn't a realistic behaviour. A ramped or smooth approach decreases these peak levels.
7. The load-displacement curves are quite similar for the spot-welded and SPR cases, except for the oscillating amplitudes.
8. Simulations at 1 m/s can be compared with static tests.

8. Further work

Further work on this model could be the investigation of:

- The influence of rivet size and geometry.
- The influence of thickness of sheets.
- The influence of other type of materials.
- The influence of cracks.
- The influence of internal stress from the rivet process.

A comparison with real tests, using the new equipment at SIMR that can perform tests at high displacement velocities.

9. References

- [1] OTTOSEN, N., PETERSSON, H., Introduction to the finite element method, Prentice Hall, (1992).
- [2] CHOPRA, ANIL K., Dynamics of structures, second edition, Prentice Hall, Inc., Upper Saddle River, New Jersey, (2000).
- [3] ABAQUS/CAE, version 6.2, Hibbitt, Karlsson & Sorensen, Inc. 2001.
- [4] ABAQUS/Explicit, version 6.2, Hibbitt, Karlsson & Sorensen, Inc. 2001.
- [5] KHEZRI, R., Finite Element Simulation of Self-Piercing Riveting of Deep Drawing and Rephosphorized Sheet Steels, Swedish Institute for Metals Research report no: IM-2000-025 (2000).
- [6] MELANDER, A., Finite element simulation of crash testing of laser welded joints, Swedish Institute for Metals Research report no: IM-2000-062 (2000).
- [7] SALEH, N., Finite element simulation of crash testing of spot welded peel specimens, Swedish Institute for Metals Research report no: IM-2002-004 (2002).
- [8] STRÖMSTEDT, E., Finite element simulation of crash testing of self-piercing rivet lap shear joint specimens, Swedish Institute for Metals Research report no: IM-2002-022 (2002).
- [9] Henrob corporation, <http://www.henrob.com>, 2002-07-04.
- [10] VOLVO Corporate Standard, STD 5531, 61.
- [11] Dokumentation 724, Untersuchungen zum Stanznieten höherfester Stahlfeinbleche, Studiengesellschaft Stahlanwendung e.V., 1998.